Long-wave radiative transfer in the middle atmosphere interacting with gravity waves and thermal tides

Masterarbeit

angefertigt am Leibniz-Institut für Atmosphärenphysik e.V. an der Universität Rostock

vorgelegt von Erik Jeglorz

Erstgutachter: Prof. Dr. Erich Becker,
Leibniz-Institut für Atmosphärenphysik e.V. an der Universität Rostock

Zweitgutachter: Dr. Urs Schaefer-Rolffs,
Leibniz-Institut für Atmosphärenphysik e.V. an der Universität Rostock

Rostock, den 25. März 2014

Abstract

This study presents an investigation of the interaction of long-wave radiative transfer with internal gravity waves and thermal tides in the middle atmosphere. Methods are based on 1) linear wave theory combined with calculations of idealized radiative transfer equations and 2) simulations with the Kühlungsborn mechanistic general circulation model (KMCM).

Wave-induced temperature perturbations lead to an increase of the net long-wave radiative cooling. Using KMCM simulations with resolved waves, we obtain maximum values for the additional net radiative cooling of 0.5 K/day for thermal tides in the equatorial lower thermosphere during equinox and 0.1 K/day for Rossby waves in the lower winter mesosphere. For strong gravity wave activity in the winter mesosphere, semi-analytical calculations yield a maximum value of 0.2 K/day. This additional cooling is significantly smaller when compared to Kutepov et al. [2007]. The discrepancy is likely caused by our too idealized description of the radiative transfer in the upper middle atmosphere.

We confirm that atmospheric gravity waves are damped due to a loss of wave energy to the radiation field. This study shows in addition that also thermal tides are subject to this mechanism. For the resolved migrating diurnal tide we demonstrate a radiative amplitude damping of about 4% when the tide propagates from the lower mesosphere up to the lower thermosphere.

Inhaltsverzeichnis

1 Introduction

1.1 Motivation

The middle atmosphere is the layer above the troposphere (lower atmosphere) and comprises the stratosphere, the mesosphere and the lower thermosphere between about 10 to 110 km height. Many exchange processes couple the lower with the middle atmosphere and are important for our understanding of tropospheric climate. One well-known example is the absorption of ultraviolet radiation due to ozone in the stratosphere. Two further important processes are long-wave radiative transfer and the role of gravity waves (GWs).

Long-wave radiative transfer is the main energy transport mechanism carrying absorbed solar radiative energy upwards through the Earth's atmosphere. It accounts for the greenhouse effect in the troposphere and balances the Earth's energy budget by emitting the same amount of radiative energy into space as is absorbed by the climate system in terms of solar radiation. In particular, long-wave radiative cooling is a first-order term in the large-scale sensible heat budget at all heights. Therefore, it has great significance for any other processes like atmospheric chemistry or atmospheric wave propagation.

Internal gravity waves can be conceived as oscillations of air parcels around their position of rest. They are mainly induced by topography, convection and wind shear in the troposphere. These waves are able to propagate from their sources into the middle atmosphere where they affect atmospheric circulation and structure. The most prominent effects are a reversal of the zonal wind jets in the mesosphere and the lower thermosphere (MLT), a warm winter stratopause and a cold summer mesopause. They are induced by a GW-driven meridional transport circulation. Thus a profound knowledge of both phenomena, radiative transfer and GW dynamics, is essential to the understanding and modeling of the middle atmosphere.

GWs with amplitudes and frequencies typical for the MLT are radiatively damped on the one hand and lead to a net increase of long-wave radiative cooling on the other. Both effects apply as well to atmospheric tides, which may be considered as forced planetary-scale gravity waves. An example for the interaction of these waves and radiative transfer is shown in Fig. 1.1. First estimates of the influence of waves on long-wave radiative transfer were provided by Fels [1982, 1984]. Recent studies by Kutepov et al. [2013, 2007] show that additional long-wave radiative cooling by GW gives a significant contribution to the heat budget in the MLT. Studies on radiative damping of GWs are rare, since there is no appropriate measurement technique and general statements from theory are hard to quantify due to the high variability of realistic GW propagation.

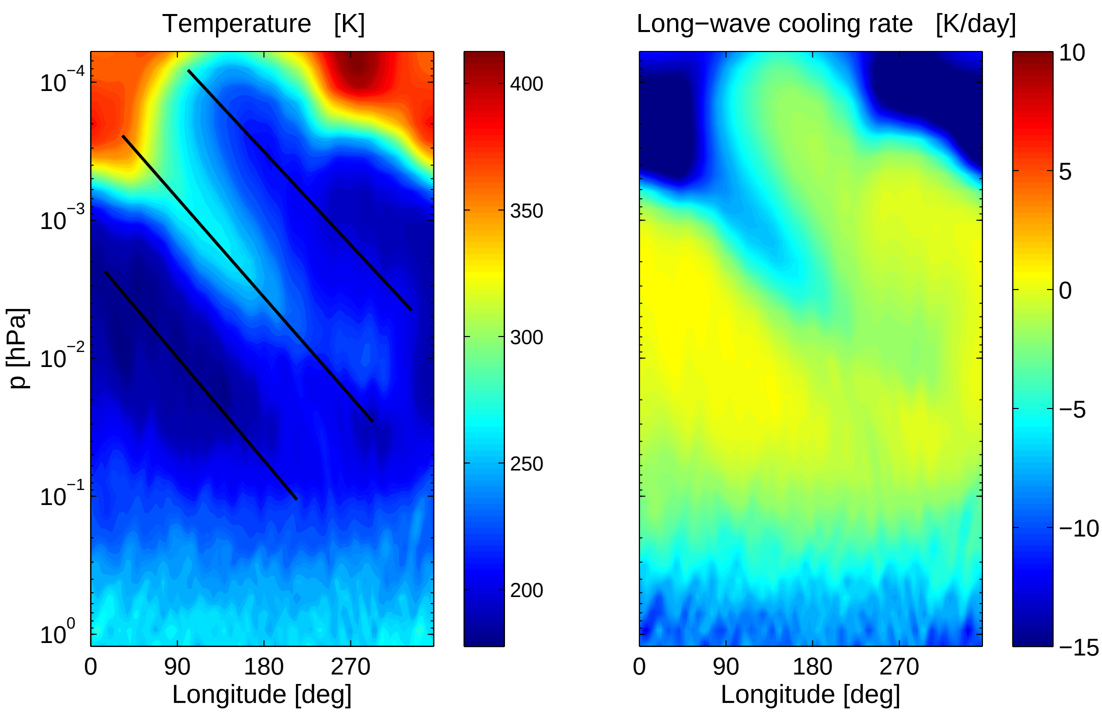

Figure 1.1: Vertical cross-sections of temperature and long-wave cooling rate at the equator in the MLT at 00:00 UT in October taken from KMCM. **Left:** A temperature perturbation generated by a strong westward propagating tide (black lines indicate phase lines). **Right:** Modulation of the long-wave cooling rate which is linked to the temperature perturbation of the tide.

Both aspects of the interaction of GWs and radiative transfer are not well resolved in modern general circulation models (GCMs) due to the fact that GWs are generally parameterized. This is necessary because the spatial scales of most GWs are smaller than the grid resolution of the climate models and that problem will last for the near future [Fritts and Alexander, 2003].

1.2 Aim

The aim of this thesis is to provide theoretical and numerical estimates of the radiative damping of GWs and thermal tides, as well as of the additional net long-wave cooling for the middle atmosphere. Model calculations are based on GCM-simulations with resolved thermal tides.

1.3 Framework

This thesis is divided into a part making use of analytical frameworks and a second one using numerical simulations. Each part covers both aspects of the interaction of waves and radiative transfer.

In the first part of this work the long-wave radiative transfer under the influence of wave-induced temperature perturbations superposed on a given background is analyzed using the two-stream approximation. Furthermore, the linearized system for GWs shall be modified by damping due to radiative transfer. The same analysis will be done for thermal tides after giving a short introduction to classical linear tidal theory.

The second part of this work contains studies of radiative wave damping and additional net cooling rates obtained from a simulation with the Kühlungsborn mechanistic general circulation model (KMCM). This climate-model version of the KMCM employs a conventional resolution such that gravity waves must be parameterized. We therefore apply the theoretical concepts derived in the first part to address the interaction of thermal tides and long-wave radiative transfer. Where possible, the conclusions are extrapolated to GWs.

2 Long-wave radiation in presence of atmospheric waves in the middle atmosphere

2.1 Basics

This section provides a brief derivation of our basic equations and mentions the most important approximations. A detailed introduction into the theory of radiative transfer is given in the text of Thomas and Stamnes [1999].

The starting point to consider radiative transfer is the *general radiative transfer equation* (RTE)

$$\frac{dI_\nu}{ds} = \rho(\vec{r},t)\,\kappa_\nu(\vec{r},t)\,(-I_\nu(\vec{r},\vec{n},t) + J_\nu(\vec{r},\vec{n},t)) \ . \tag{2.1}$$

Here, I_ν is the spectral intensity, κ_ν the spectral mass extinction coefficient, J_ν the spectral source function and ρ the density. $\vec{n}$ describes the directional dependence. Equation (2.1) is a macroscopic balance equation including absorption, scattering and emission.

The general RTE contains unknown dependencies that have to be specified. This is done by using the following approximations:

- A common approximation is local thermodynamic equilibrium (LTE), meaning that the population of radiatively active energy levels of molecules in the thermal regime follows the Maxwell-Boltzmann-distribution, i.e., they are determined by collisions. In this case we identify

$$J_\nu(\vec{r},t) = B_\nu(\vec{r},t) \tag{2.2}$$

  with B_ν being the Planck-function. Scattering in the source function vanishes in LTE-approximation by definition.

- In plane-parallel approximation the dependencies on longitude and latitude are neglected. Furthermore, we retain only the directional dependence of the intensity on the zenith angle ϑ. This leads to

$$J_\nu(\vec{r},t) = B_\nu(z,t) \tag{2.3}$$

$$I_\nu(\vec{r},\vec{n},t) \to I_\nu(z,\vartheta,t) \tag{2.4}$$

- We further parameterize the dependence on ϑ using the two-stream approximation:

$$I_\nu(\vartheta) = \begin{cases} I_\nu^+ & 0 \le \vartheta \le \frac{\pi}{2} \\ I_\nu^- & \frac{\pi}{2} \le \vartheta \le \pi \end{cases} \tag{2.5}$$

  Thus I^+ indicates the intensity directed in the upper half space and I^- the intensity directed in the lower half space.

- Our next assumption is known as 'gray limit' and assumes that frequency variations of the extinction coefficient within a wide frequency range can be neglected.

- Long-wave or thermal radiation refers to radiation in the wavelength range from about $5\,\mu$m to $100\,\mu$m absorbed and emitted by air parcels and the Earth's surface. As shown in the top panel of Fig. 2.1 this range covers mostly the black-body curve for $T = 250$ K. A comparison with the bottom panel of Fig. 2.1 reveals four dominant long-wave absorber bands: H_2O around $6.3\,\mu$m, O_3 around $9.6\,\mu$m, CO_2 around $15\,\mu$m and H_2O-rotation for $\lambda > 20\,\mu$m. Therefore, an infinite broad band is a strong approximation. We nevertheless use this idealization for analytical estimates. Together with the two-stream approximation the broad-band approximation can be written as

$$\int_0^\infty \kappa_\nu\, I_\nu(\vartheta)\, d\nu = \begin{cases} \kappa\, I^+ & 0 \le \vartheta \le \frac{\pi}{2} \\ \kappa\, I^- & \frac{\pi}{2} \le \vartheta \le \pi \end{cases} \tag{2.6}$$

$$\int_0^\infty \kappa_\nu B_\nu\, d\nu = \frac{\kappa\,\sigma T^4}{\pi}\,. \tag{2.7}$$

  Here, κ is a height dependent mass extinction coefficient, T the temperature and σ the Stefan-Boltzmann constant.

So far we have

$$\cos\vartheta\,\frac{dI}{dz} = \rho\,\kappa\,(-I + \frac{2\,\sigma\,T^4}{\pi})\,. \tag{2.8}$$

Integrating (2.8) over the upper and lower half space,

$$\int_\Omega \cos\vartheta\, I^+\, d\Omega\; = \frac{\pi}{2}\, I^+ = U\,, \qquad \int_\Omega \cos\vartheta\, I^-\, d\Omega\; = \frac{\pi}{2}\, I^- = D\,, \tag{2.9}$$

leads to two first order differential equations, namely for the upward and the downward radiative energy fluxes:

$$\frac{\partial U}{\partial z} = +2\,\kappa\,\rho\,(-U + \sigma\,T^4)\,, \tag{2.10}$$

$$\frac{\partial D}{\partial z} = -2\,\kappa\,\rho\,(-D + \sigma\,T^4)\,. \tag{2.11}$$

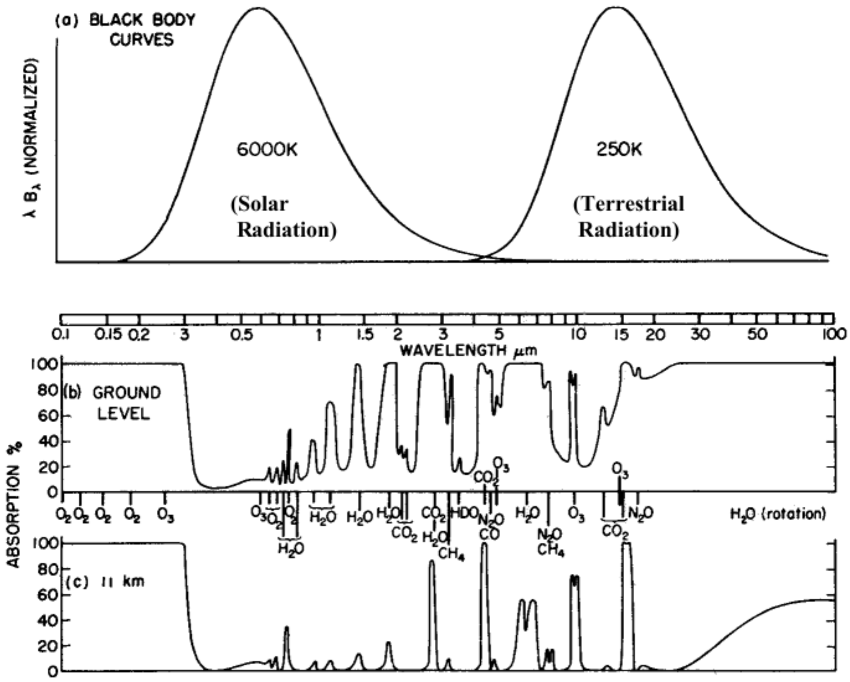

Figure 2.1: As a function of wavelength: (**top**) normalized spectral intensity of a black body for 6000 K and 250 K, (**middle**) atmospheric absorption spectrum for a solar beam reaching ground level and (**bottom**) atmospheric absorption spectrum for a solar beam reaching the tropopause. (From [Thomas and Stamnes, 1999])

2.2 Solving the two-stream RTEs

Equation (2.10) and (2.11) are simplified RTEs such as to allow for analytical solutions. Taking the boundary conditions $U(z=0) = \sigma T_\mathrm{s}^4$ and $D(z \to \infty) = 0$ into account, we can solve the equations for U and D by summing up their homogeneous and inhomogeneous solutions.

With separation of variables and integration we find the homogeneous solution of Eq. (2.10)

$$\frac{dU_\mathrm{h}}{dz} = -2\,\kappa\,\rho\,U_\mathrm{h} \qquad \rightarrow \qquad U_\mathrm{h} = U_\mathrm{h}(0)\cdot\exp\left\{-2\int_0^z \kappa\,\rho\,dz'\right\} \tag{2.12}$$

For the inhomogeneous equation we choose a particular ansatz so that $U_\mathrm{ih}(z=0) = 0$

$$U_\mathrm{ih} = \int_0^z 2\,\kappa\,\rho\,f(z,z')\,\sigma\,T^4\,dz'\,. \tag{2.13}$$

Now we seek the unknown function $f(z,z')$. The partial derivative of the ansatz with respect to z using the Leibniz integration rule is on the one hand

$$\frac{dU_\mathrm{ih}}{dz} = \int_0^z \frac{d}{dz} 2\,\kappa\,\rho\,f(z,z')\,\sigma\,T^4\,dz' + 2\,\kappa\,\rho\,f(z,z)\,\sigma\,T^4 \tag{2.14}$$

and applying the ansatz to Eq. (2.10) on the other

$$\frac{dU_{\mathrm{ih}}}{dz} = -2\,\kappa(z)\,\rho(z)\int_0^z 2\,\kappa\,\rho\,f(z,z')\,\sigma\,T^4\,dz' + 2\,\kappa\,\rho\,\sigma\,T^4\,. \tag{2.15}$$

Comparing both results yields $f(z,z) = 1$. It is important to strictly distinguish the dependencies of κ, ρ, T and f on z, z' and z''. Subtracting Eq. (2.14) from (2.15) results in

$$\int_0^z \left\{\frac{d}{dz} 2\,\kappa(z')\,\rho(z')\,f(z,z')\,\sigma\,T^4(z') \; + 2\,\kappa(z)\,\rho(z)\,2\,\kappa(z')\,\rho(z')\,f(z,z')\,\sigma\,T^4(z')\right\} dz' = 0\,. \tag{2.16}$$

The upper integration boundary z is arbitrary. Canceling $\kappa(z')\,\rho(z')\,\sigma\,T^4(z')$, Eq. (2.16) thus becomes

$$\frac{d}{dz} f(z,z') \; + 2\,\kappa(z)\,\rho(z)\,f(z,z') = 0\,. \tag{2.17}$$

Separation of variables and integration from z' to z leads to

$$f(z,z') = \exp\left\{2\int_z^{z'} \kappa\,\rho\,dz''\right\}\,. \tag{2.18}$$

The overall solution reads

$$U = U_{\mathrm{h}} + U_{\mathrm{ih}} = U(z_s)\cdot\exp\left\{-2\int_0^z \kappa\,\rho\,dz'\right\} + \int_0^z 2\,\kappa\,\rho\,\exp\left\{2\int_z^{z'} \kappa\,\rho\,dz''\right\}\sigma\,T^4\,dz'\,. \tag{2.19}$$

In the same manner it is possible to find the solution for D. Differences arise from the boundary conditions.

$$U = \sigma\,T_s^4 \cdot \exp\left\{-2\int_0^z \kappa\,\rho\,dz'\right\} \qquad + \int_0^z 2\,\kappa\,\rho\,\exp\left\{2\int_z^{z'} \kappa\,\rho\,dz''\right\}\sigma\,T^4\,dz' \tag{2.20}$$

$$D = \qquad\qquad - \int_\infty^z 2\,\kappa\,\rho\,\exp\left\{-2\int_z^{z'} \kappa\,\rho\,dz''\right\}\sigma\,T^4\,dz'\,. \tag{2.21}$$

For D the homogeneous solution vanishes, because there is no incoming long-wave radiation from space.

2.3 Definition of the cooling rate

The impact of radiative transfer on an air parcel is heating (prevailing absorption) or cooling (prevailing emission). The physical quantity is the cooling rate

$$Q_{\mathrm{rad}} = -\frac{1}{\rho}\,\partial_{\mathrm{z}}\,(U - D). \tag{2.22}$$

Applying the RTEs (2.10) and (2.11) to this definition yields

$$Q_{\mathrm{rad}} = 2\,\kappa\,(U + D - 2\,\sigma\,T^4)\,. \tag{2.23}$$

From this point of view the cooling rate is the difference between the absorbed upward and downward energy flux on the one hand and the long-wave flux, which a layer emits by itself, on the other hand. Although Q_{rad} is a heating rate by definition, the term cooling rate is used throughout this work. A negative Q_{rad} means cooling.

In the case of long-wave radiation, negative Q_{rad} (sum over all bands) prevails throughout the atmosphere. An exception has to be made around the cold mesopause where long-wave radiative heating can occur. Short-wave radiation from the sun is related to heating, especially around the stratopause and in the thermosphere.

2.4 Cooling rate with non-LTE

Above about 50 km the assumption that the population of energy levels of air molecules are determined only by collision rates inside the gas becomes increasingly inaccurate. The collision rates are proportional to density, which is decreasing exponentially with altitude. Spontaneous emission also gains importance. The overall effect is a decrease of vibrational and rotational transition rates (meaning a smaller number of absorption and emission processes for each molecule). The declining transfer between kinetic and radiation energy with increasing altitude is called the break down of LTE or shortly non-LTE.

The non-LTE effect may be modeled by an additional factor $(1-\omega_{\mathrm{s}})$ in Eq. (2.23) describing reduced absorption and emission efficiency as an increasing scattering efficiency

$$Q_{\mathrm{rad}} = 2\,\kappa\,(1 - \omega_{\mathrm{s}})\,(U + D - 2\,\sigma\,T^4)\,. \tag{2.24}$$

ω_{s} is the scattering albedo. Equation (2.24) can also be derived, if scattering is incorporated from the beginning as a part of the source function J_ν. As a consequence Eqs. (2.10) and (2.11) would expand to

$$\frac{\partial U}{\partial z} = +\kappa\,\rho\,(-2\,U + \omega_{\mathrm{s}}\,U + \omega_{\mathrm{s}}\,D + 2\,(1-\omega_{\mathrm{s}})\,\sigma\,T^4)\,, \tag{2.25}$$

$$\frac{\partial D}{\partial z} = -\kappa\,\rho\,(-2\,D + \omega_{\mathrm{s}}\,U + \omega_{\mathrm{s}}\,D + 2\,(1-\omega_{\mathrm{s}})\,\sigma\,T^4)\,. \tag{2.26}$$

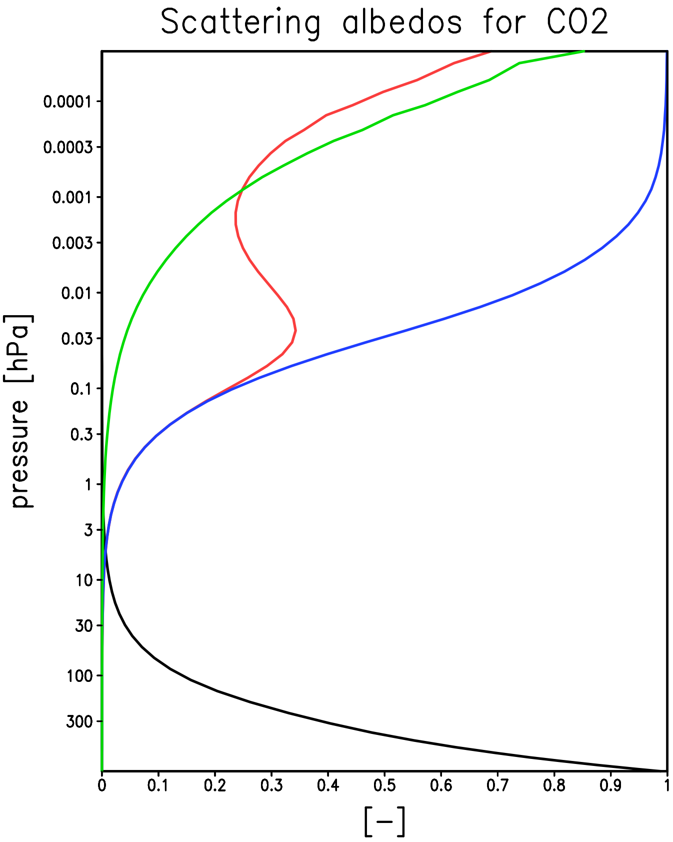

Figure 2.2: Scattering albedos for CO_2: (red) global annual mean from KMCM, (blue) original parameterization from Eq. (2.27) and (green) adjusted parameterization (see text). The ratio ρ/ρ_s is given by the black line.

To show that we can nevertheless proceed with Eqs. (2.10) and (2.11) and that their integral formulation remains valid, the actual vertical profile of ω_s has to be considered. CO_2 contributes mostly to the total cooling rate in the atmosphere above 30 km. Thus, the description of the non-LTE effect due to CO_2 is assumed to be a good representation of this effect for the MLT in general. A common idealization for the scattering albedo is

$$\omega_s = \frac{A_{21}}{A_{21} + c_{21}} = \frac{1}{1 + \frac{c_{21,s}}{A_{21}} \frac{\rho}{\rho_s}} \,. \tag{2.27}$$

Here, $1/A_{21} = 0,74$ s is the inverse Einstein coefficient due to spontaneous emission and $1/c_{21,s} = 3 \cdot 10^{-5}$ s is the inverse collision rate. The index s denotes values of C_{21} and ρ at the Earth's surface. Fig. 2.2 shows scattering albedos. The difference between the more realistic ω_s of KMCM and formula (2.27) is caused by the additional consideration of inelastic collisions of CO_2 with atomic oxygen. For our idealized approach we proceed with a slight modification of the scattering albedo (green line). It is modeled with a slower decrease in density in Eq. (2.27).

An important feature illustrated in the figure is the opposite dependence of density and scattering albedo on altitude. Therefore, the terms proportional to ω_s on the right-hand sides of Eqs. (2.25) and (2.26) vanish below 50 km due to ω_s. Above, the density has dropped by more than three orders of magnitude and changes in U and D are extremely small compared to those taking place in the column below. The formal result is that the computation of U and D in the MLT can still be performed on the basis of Eqs. (2.10) and (2.11). This holds as long as U and D are non-local quantities, meaning the bulk of the long-wave radiation is emitted below the MLT. This point will be discussed more in detail when turning to wave perturbations of U and D.

2.5 Temporal and zonal average

A common tool to distinguish physical processes on different spatial or temporal scales is splitting the quantity X in a reference value X_r and a disturbance X'

$$X = X_\mathrm{r} + X'. \tag{2.28}$$

X_r can be defined either by temporal average

$$X_\mathrm{r} = \langle X \rangle = \frac{1}{\tau} \int_0^\tau X(t)\,dt\,, \quad \langle X' \rangle = 0\,, \tag{2.29}$$

or by zonal (or meridional) average

$$X_\mathrm{r} = [X] = \frac{1}{x_\mathrm{b} - x_\mathrm{a}} \int_{x_\mathrm{a}}^{x_\mathrm{b}} X(x)\,dx\,, \quad [X'] = 0\,. \tag{2.30}$$

In the following a background atmosphere is described by zonally and temporally averaged quantities indicated by index r. Wave disturbances are indicated by a prime. To simplify the notation, we drop the meridional dependence y and thus define

$$\{p, \rho, T, U, D\}\,(x, z, t) = \{p_\mathrm{r}, \rho_\mathrm{r}, T_\mathrm{r}, U_\mathrm{r}, D_\mathrm{r}\}\,(z) + \{p', \rho', T', U', D'\}\,(x, z, t)\,. \tag{2.31}$$

In order to make the radiation calculation analytically feasible, we assume the background temperature being constant with altitude. This approximation will lead to some significant deviations from more realistic numerical calculations. It will be shown that the most important analytical results are nevertheless quantitatively reasonable when compared to numerical solutions.

From hydrostatic balance $\partial_z p_\mathrm{r} = -g\,\rho_\mathrm{r}$ and the ideal gas law $p_\mathrm{r} = \rho_\mathrm{r}\,R\,T_\mathrm{r}$ the background density ρ_r yields

$$\rho_\mathrm{r}(z) = \rho_\mathrm{s} \cdot e^{-z/H}\,, \tag{2.32}$$

with H being the scale height $H = R\,T_\mathrm{r}/g$.

Wave type	vertical wavelength [km]	T_a [K]	T'_max [K]	z_crit [km]	$1/l_\mathrm{diss}$ [1/m]
Excessive	10	10	±100	40	$4 \cdot 10^{-4}$
GW	10	0.075	±25	90	$4 \cdot 10^{-4}$
TW	28	0.135	±60	95	$8 \cdot 10^{-5}$
RW	40	1.1	±25	55	$1.3 \cdot 10^{-4}$

Table 2.1: Parameters for a monochromatic excessive wave, gravity wave (GW), tidal wave (TW) and (forced) Rossby wave (RW) used in all following figures.

2.6 Radiative transfer with a wave disturbance

Applying Eq. (2.32) to (2.20) and (2.21), and assuming a constant κ, the integrals in the exponential function can be solved. The energy fluxes become

$$\begin{aligned} U(z) = &\sigma T_s^4 \cdot \exp\{2\kappa H(\rho_\mathrm{r}(z) - \rho_{00})\} \\ &+ 2\kappa \int_0^z \rho_\mathrm{r}(z') \exp\{2\kappa H(\rho_\mathrm{r}(z) - \rho_\mathrm{r}(z'))\}\, \sigma T^4(z')\, dz' \end{aligned} \tag{2.33}$$

$$D(z) = -2\kappa \int_\infty^z \rho_\mathrm{r}(z') \exp\{2\kappa H(\rho_\mathrm{r}(z') - \rho_\mathrm{r}(z))\}\, \sigma T^4(z')\, dz' \tag{2.34}$$

These equations are evaluated, first of all, in the presence of an excessive wave. After the general features are clarified, reasonable monochromatic temperature perturbations due to a GW, a tidal wave (TW) and a (forced) Rossby wave (RW) are also applied. We assume for all waves a sine-shaped disturbance T' of the form

$$T' = T_a\, S(z, z_c)\, \exp\left\{\frac{z}{2H} + i(k\,x + m\,z - \omega\,t)\right\}, \tag{2.35}$$

$$S(z, z_c) = \frac{1}{1 + \exp\left\{\frac{z - z_c}{l_{diss}}\right\}}. \tag{2.36}$$

The factor $\exp\left\{\frac{z}{2H}\right\}$ arises from conservation of wave energy density with altitude. The sigmoid function S models dissipation processes. The parameter z_c marks the central altitude of these processes and l_diss is a length scale that measures how fast the waves decline. The parameters of the waves that are shown in all following figures are listed in Table 2.1. If not mentioned otherwise, we use $T_\mathrm{r} = 245$ K, $T_\mathrm{s} = 270$ K and $\kappa = 0.00015$ $\mathrm{m^2/kg}$.

Fig. 2.3 shows the effect of an exaggerated wave disturbance on the energy fluxes according to Eq. (2.33) and (2.34). A direct connection between a temperature maximum due to the wave and an increase of energy fluxes can be identified. This increase is for U above and for D below the altitude of the maximum T' and vice versa for temperature minima. It can also be seen that the total amount of upward energy flux is increased compared to the reference state. Since D vanishes at the top of the atmosphere (TOA), the atmosphere undergoes an additional loss of radiation energy into space. A wave

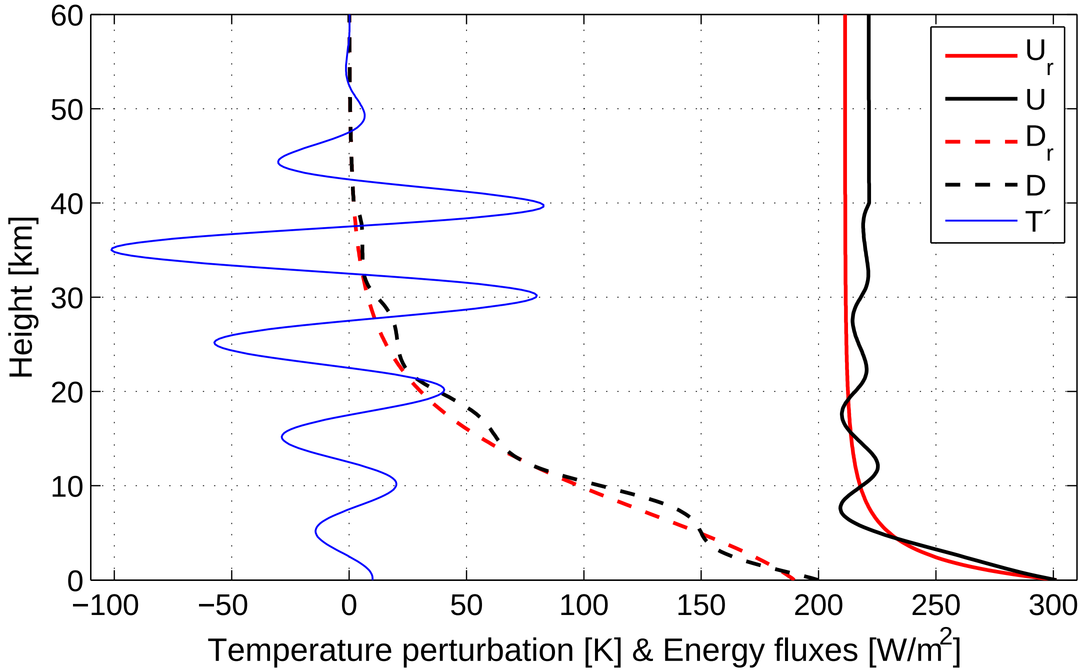

Figure 2.3: Vertical cross-section of upward and downward long-wave radiative energy fluxes for: (red) an isothermal background atmosphere and (black) an isothermal background atmosphere with an additional excessive wave disturbance T' (blue).

variation in U and D is visible only at lower altitudes, especially in the troposphere and lower stratosphere. An estimation of the effect on U and D due to a GW, a TW and a RW is depicted in Fig. 2.4. For the GW and TW there are no visible changes in U and D with the wave perturbation included (U_{GW}, U_{TW}, D_{GW}, D_{TW}) when compared to the result for just the reference state (U_{r}, D_{r}). Indeed, the deviations do not exceed 0.2 W/m^2 over the whole altitude range. This is not fully true for the RW. Small deviations between U_{r} and U_{RW} are located below 40 km. The energy fluxes are changed up to 3 W/m^2 for our example but alterations could be larger for a RW with stronger amplitudes and more concentrated in the lower troposphere.

2.7 Simplified cooling rate

We expand the T^4 term and truncate the power series at $j = 2$

$$(T_{\mathrm{r}} + T')^4 = \sum_{j=0}^{4} \binom{4}{j} T_{\mathrm{r}}^{j}\, T'^{4-j} \tag{2.37}$$

$$\approx T_{\mathrm{r}}^4 + 4\,T_{\mathrm{r}}^3\,T' + 6\,T_{\mathrm{r}}^2\,T'^2. \tag{2.38}$$

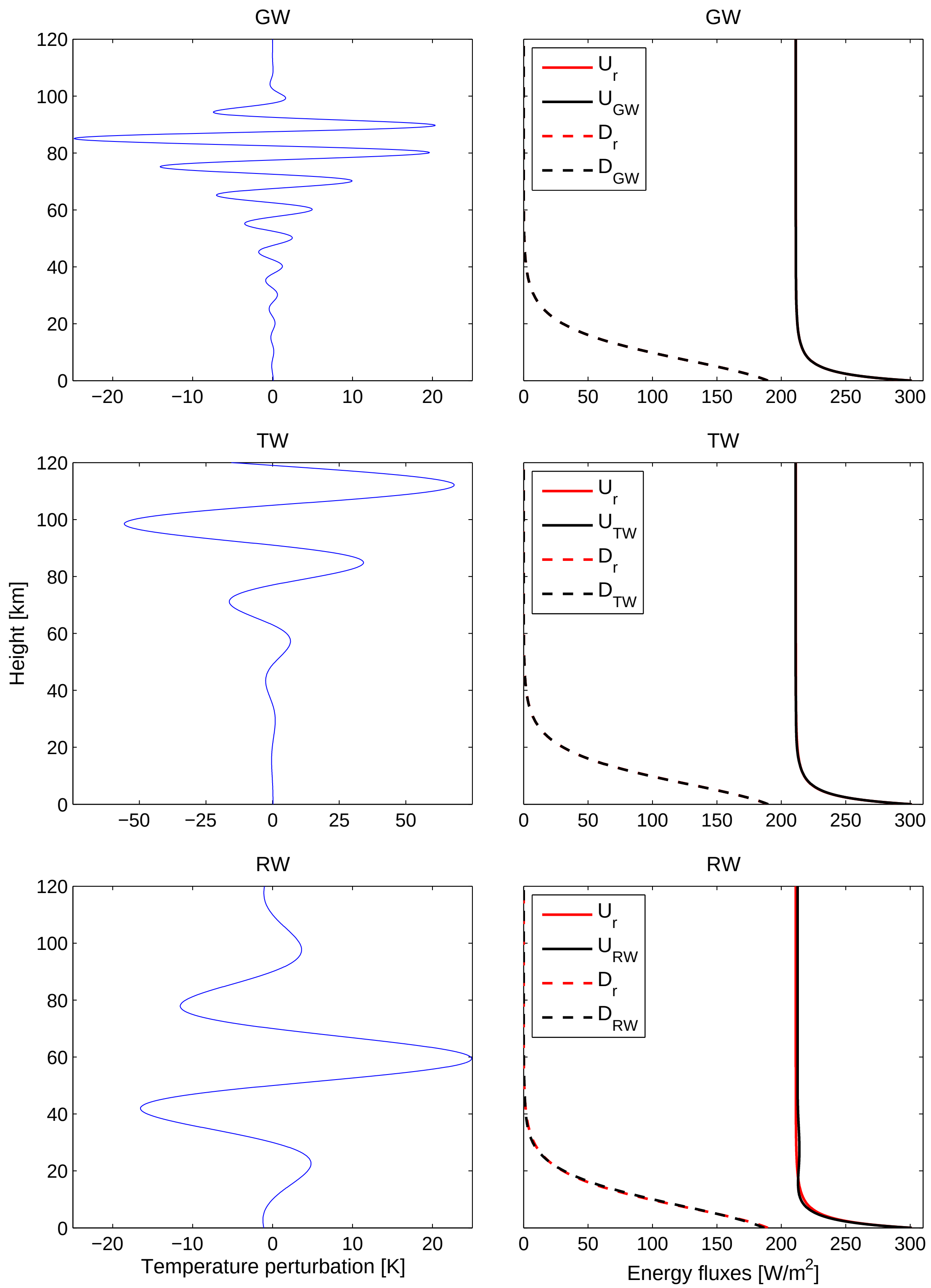

Figure 2.4: Left: Possible temperature disturbances due to a monochromatic GW, TW and RW. **Right:** Long-wave radiative energy fluxes (black) with and (red) without the temperature disturbance (on the left-hand side) for an isothermal background atmosphere. For the RW a slight difference between U_r and U_RW is visible. In case of a GW and TW, U_r and D_r are hidden below the almost identical energy fluxes U_GW, U_TW, D_GW, D_TW.

Inserting into the energy flux equations (2.33) and (2.34) leads to

$$\begin{aligned}
U = & \underbrace{\sigma\, T_s^4\, \exp\left\{2\,\kappa\, H\,(\rho_\mathrm{r} - \rho_{00})\right\} + 2\,\kappa \int_0^z \rho_\mathrm{r}(z')\, \exp\left\{2\,\kappa\, H\,(\rho_\mathrm{r}(z) - \rho_\mathrm{r}(z'))\right\}\, \sigma\, T_\mathrm{r}^4\, dz'}_{=U_\mathrm{r}(z)} \\
& + \underbrace{2\,\kappa \int_0^z \rho_\mathrm{r}(z')\, \exp\left\{2\,\kappa\, H\,(\rho_\mathrm{r}(z) - \rho_\mathrm{r}(z'))\right\}\, \sigma\, 4\, T_\mathrm{r}^3\, T'(z')\, dz'}_{=U'(z)} \\
& + \underbrace{2\,\kappa \int_0^z \rho_\mathrm{r}(z')\, \exp\left\{2\,\kappa\, H\,(\rho_\mathrm{r}(z) - \rho_\mathrm{r}(z'))\right\}\, \sigma\, 6\, T_\mathrm{r}^2\, T'^2(z')\, dz'}_{=U''(x,z,t)}\,,
\end{aligned} \tag{2.39}$$

$$\begin{aligned}
D = & \underbrace{-2\,\kappa \int_\infty^z \rho_\mathrm{r}(z')\, \exp\left\{2\,\kappa\, H\,(\rho_\mathrm{r}(z') - \rho_\mathrm{r}(z))\right\}\, \sigma\, T_\mathrm{r}^4\, dz'}_{=D_\mathrm{r}(z)} \\
& \underbrace{-2\,\kappa \int_\infty^z \rho_\mathrm{r}(z')\, \exp\left\{2\,\kappa\, H\,(\rho_\mathrm{r}(z') - \rho_\mathrm{r}(z))\right\}\, \sigma\, 4\, T_\mathrm{r}^3\, T'(z')\, dz'}_{=D'(x,z,t)} \\
& \underbrace{-2\,\kappa \int_\infty^z \rho_\mathrm{r}(z')\, \exp\left\{2\,\kappa\, H\,(\rho_\mathrm{r}(z') - \rho_\mathrm{r}(z))\right\}\, \sigma\, 6\, T_\mathrm{r}^2\, T'^2(z')\, dz'}_{=D''(x,z,t)}\,.
\end{aligned} \tag{2.40}$$

Double primes indicate a dependency on a product of two disturbance quantities. The cooling rate formula expands to

$$\begin{aligned}
Q_\mathrm{rad}(x,z,t) \approx & \underbrace{2\,\kappa\,(1-\omega_\mathrm{s})\,(U_\mathrm{r} + D_\mathrm{r} - 2\,\sigma\, T_\mathrm{r}^4)}_{=Q_\mathrm{rad,r}(z)} + \underbrace{2\,\kappa\,(1-\omega_\mathrm{s})\,(U' + D' - 8\,\sigma\, T_\mathrm{r}^3\, T')}_{=Q'_\mathrm{rad}(x,z,t)} \\
& + \underbrace{2\,\kappa\,(1-\omega_\mathrm{s})\,(U'' + D'' - 12\,\sigma\, T_\mathrm{r}^2\, T'^2)}_{=Q''_\mathrm{rad}(x,z,t)}
\end{aligned} \tag{2.41}$$

From Fig. 2.4 it is found that the quantities U', D', U'' and D'' are very small for a GW and a TW. This becomes evident when considering U' in Eq. (2.39). Starting close to zero in the troposphere, T' increases with $\exp(z/2H)$ but is overcome by the decreasing density $\rho_\mathrm{r} \propto \exp(-z/H)$, hence $U' \to 0$ for $z \to \infty$ as long as κ exhibits no exponential growth with altitude.

This simple consideration is in contrast to the idea of scale-dependent radiative cooling rates in the middle atmosphere as suggested by Fels [1982] or Zhu [1993]. These authors state that the radiative cooling of an air layer is affected by the vertical spatial scales of adjacent temperature perturbations - e.g. a warm layer should cool more when sandwiched by cool layers, as in the case for GWs.

At this point one may raise the question how strongly a realistic frequency averaged κ, which is in general a function of temperature and density, varies with height? We found that these variations are negligible in comparison to the exponential decay of the density itself. For example, the frequency averaged κ of the important CO_2 15 μm band

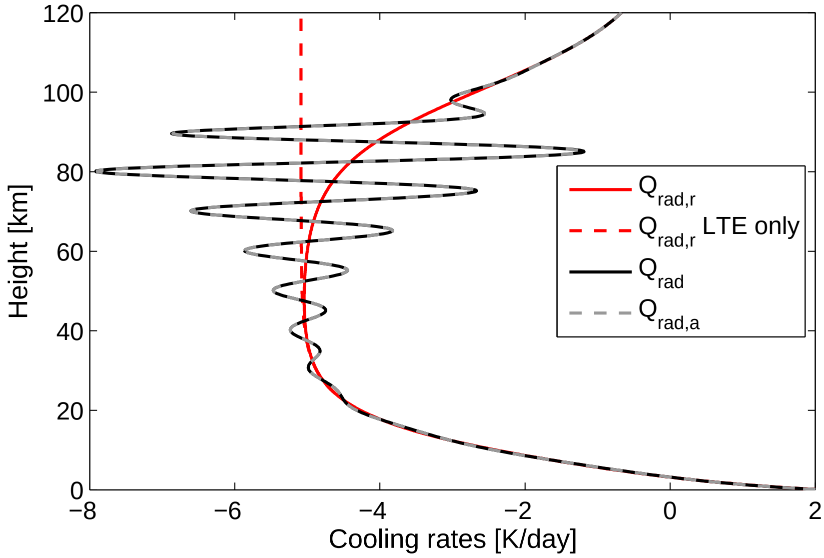

Figure 2.5: Cooling rates for an isothermal background state (red) with and (red dashed) without consideration of non-LTE. Including a GW disturbance, cooling rates are calculated for (black solid) retaining and (grey dashed) omitting terms of U', D', U'' and D''. There is no visible difference. It can be noted that cooling by the wave with respect to $Q_{\mathrm{rad,r}}$ is slightly higher than heating.

fluctuates by less than 30% throughout the middle atmosphere; see [Knöpfel and Becker, 2011] and Fig. A.1 in the appendix. Therefore, a relevant effect of adjacent layers on each other by long-wave radiative transfer is not likely to exist in the MLT. This result, supported also by Kutepov et al. [2007][1], contradicts the finding of Zhu [1993] that the importance of scale-dependence should increase up to 80 km. In conclusion, U', D', U'' and D'' can be omitted for GWs and TWs and the additional cooling rate is given by $Q'_{\mathrm{rad}} + Q''_{\mathrm{rad}}$, where

$$Q'_{\mathrm{rad}} \approx -16\,\kappa\,\sigma\,(1-\omega_{\mathrm{s}})\,T_{\mathrm{r}}^{3}\,T'\,, \tag{2.42}$$

$$Q''_{\mathrm{rad}} \approx -24\,\kappa\,\sigma\,(1-\omega_{\mathrm{s}})\,T_{\mathrm{r}}^{2}\,T'^{\,2}\,. \tag{2.43}$$

The complete cooling rate reads

$$Q_{\mathrm{rad}}(x,z,t) = 2\,\kappa\,(1-\omega_{\mathrm{s}})\,(U_{\mathrm{r}} + D_{\mathrm{r}} - 2\,\sigma T_{\mathrm{r}}^{4} - 8\,\sigma\,T_{\mathrm{r}}^{3}\,T' - 12\,\sigma\,T_{\mathrm{r}}^{2}\,T'^{\,2})\,, \tag{2.44}$$

$$U_{\mathrm{r}} = \sigma\,T_{\mathrm{s}}^{4}\,\exp\{2\,\kappa\,H\,(\rho_{\mathrm{r}}-\rho_{00})\} + \sigma\,T_{\mathrm{r}}^{4}\,(1-\exp\{2\,\kappa\,H\,(\rho_{\mathrm{r}}-\rho_{00})\})\,,$$

$$D_{\mathrm{r}} = \sigma\,T_{\mathrm{r}}^{4}\,(1-\exp\{-2\,\kappa\,H\,\rho_{\mathrm{r}}\}).$$

2.8 Cooling rate with wave disturbance

The impact of a wave on the cooling rate is determined by evaluating Eq. (2.44). In Fig. 2.5 it can be seen that the additional cooling and heating of the GW is added to the (predominant) cooling of the background state. Temperature changes due to the wave appear instantaneously in the cooling rates. The cooling rates, including wave disturbances, are calculated for both retaining and omitting terms of U', D', U'' and D''. The latter is the analytical solution $Q_{\mathrm{rad,a}}$ from Eq. (2.44) whereas the full solution Q_{rad} is calculated numerically from Eq. (2.41). There is a perfect coincidence between both solutions. Note that $Q_{\mathrm{rad,r}}$ is somewhat unrealistic due to the isothermal temperature profile of the background. Taking the non-LTE effect into account is necessary for describing cooling rates in the MLT properly.

2.9 Cooling rates in the temporal mean

The cooling rates given in Fig. 2.5 represent only a snapshot of the current state of the atmosphere. The periods of GWs reach from 5 min to a maximum of 10 – 15 h. For the most important thermal tides the periods are 8, 12 and 24 h. These are much smaller time scales as considered for the climatological mean. Therefore, we examine the net effect of additional cooling rates by taking the temporal mean of Eq. (2.44). The only time-dependent quantity is T'. Introducing a definition for the wave amplitude

$$\widehat{T}' := T_a\, S\, \exp\left\{\frac{z}{2\,H}\right\}, \tag{2.45}$$

we have

$$\langle T' \rangle = \frac{\widehat{T}'}{\tau} \int_0^\tau \cos^{\mathbf{1}}(\omega\, t + \varphi)\, dt = 0\,, \tag{2.46}$$

$$\left\langle T'^{\,2} \right\rangle = \frac{\widehat{T}'^{\,2}}{\tau} \int_0^\tau \cos^{\mathbf{2}}(\omega\, t + \varphi)\, dt = \frac{\widehat{T}'^{\,2}}{2}\,. \tag{2.47}$$

Here, τ is a multiple of the wave period and φ an arbitrary phase. The climatological relevant part of the additional cooling rate is, therefore, a second-order effect and reduces to

$$\langle Q''_{\mathrm{rad}} \rangle = -12\,\kappa\,\sigma\,(1-\omega_{\mathrm{s}})\,T_{\mathrm{r}}^2\,\widehat{T}'^{\,2}\,. \tag{2.48}$$

The same conclusion can be made by taking the zonal average being necessary for global stationary RWs. The net cooling rate is given by

$$\langle Q_{\mathrm{rad}}(z) \rangle = 2\,\kappa\,(1-\omega_{\mathrm{s}})\,(U_{\mathrm{r}} + D_{\mathrm{r}} - 2\,\sigma T_{\mathrm{r}}^4 - 6\,\sigma\,T_{\mathrm{r}}^2\,\widehat{T}'^{\,2})\,. \tag{2.49}$$

[1] "... the non-local integral heating term J is less sensitive to the increase of the local temperature because of the contribution of the upward radiation fluxes, which are less affected by the ITFs in the lower atmosphere.", (ITF): Irregular temperature fluctuations due to GWs

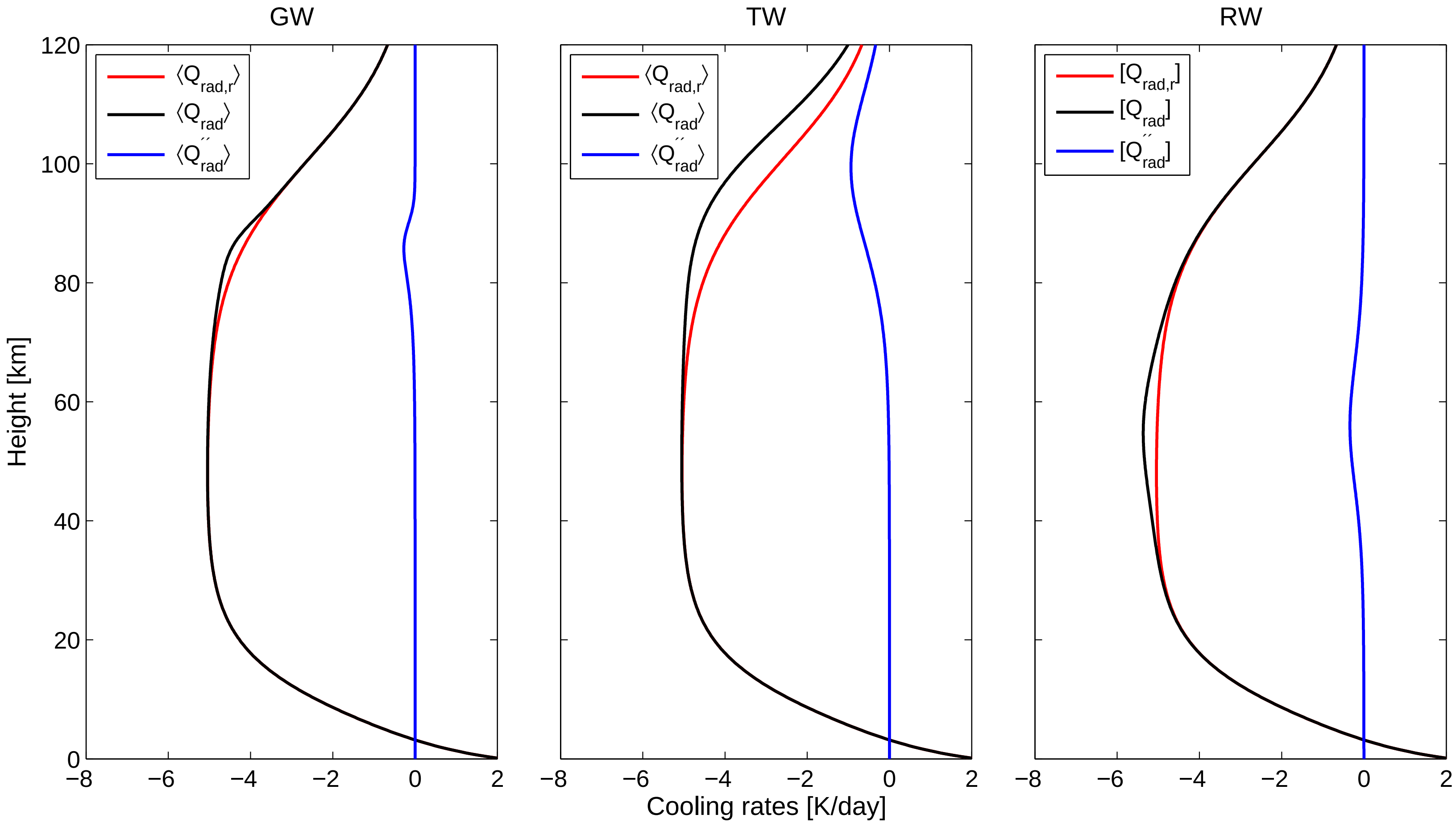

Figure 2.6: Temporal (or zonal for the RW) averaged radiative cooling rates for the GW, TW and RW (left to right) for an isothermal atmosphere. For each wave it is calculated (red) the cooling rate of the background atmosphere, (black) the net cooling rate including wave disturbances and (blue) the additional net cooling rate. The max. values of $|Q''_{\mathrm{rad}}|$ are 0.27 K/day for the GW, 0.95 K/day for the TW and 0.33 K/day for the RW.

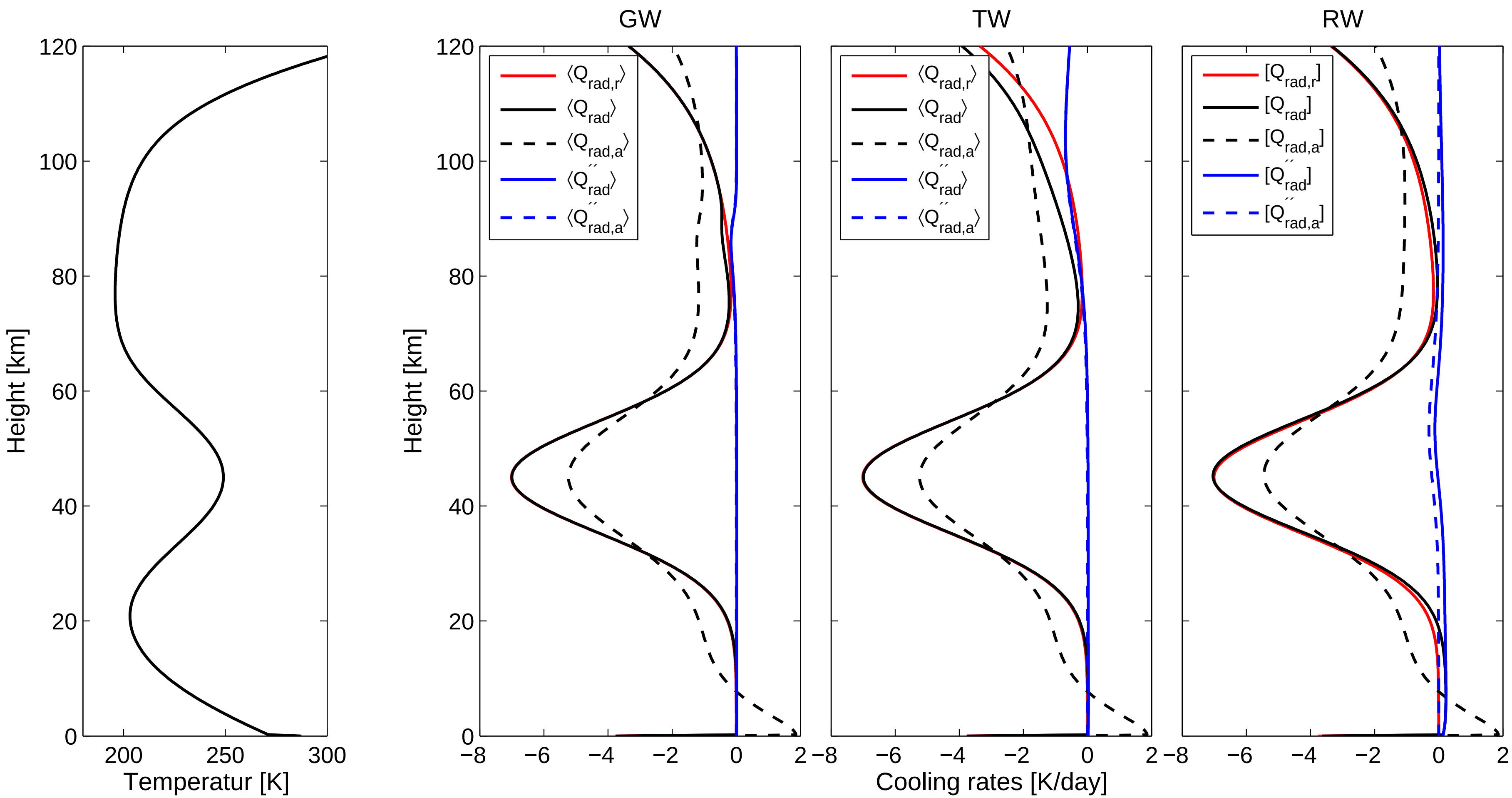

Figure 2.7: Left: Temperature profile representing a global annual mean that is used for the cooling rate calculations. **Right:** Temporal (or zonal for the RW) averaged radiative cooling rates for the GW, TW and RW in the non-isothermal atmosphere. For each wave it is calculated (red) the cooling rate of the background atmosphere, (black) the net cooling rate including wave disturbances and (blue) the additional net cooling rate. Dashed lines represent analytical approximations (Eqs. (2.48) and (2.49)) and solid lines numerical exact results (using Eq. (2.24)).

Equation (2.49) has some remarkable properties. There are no dependencies on vertical wave number and frequency. The remaining wave property is the amplitude $\widehat{T}'$. Both the wave amplitude and the background temperature are the most important factors for producing high additional cooling rates. From that point of view we would expect large $\langle Q''_{\mathrm{rad}} \rangle$ around the stratopause and the lower thermosphere in combination with strong wave activity. Wave filtering and dissipative processes determine which parts of the wave spectrum launched at lower altitudes may reach those regions in the middle atmosphere. Therefore, wave-induced radiative cooling is expected to be variable in space and time. In Chap. 4 we will analyze numerical simulations with the KMCM in order to estimate where resolved RWs and TWs may lead to additional radiative cooling.

Figure 2.6 gives an overview of the additional averaged cooling caused by the different wave types calculated from Eq. (2.49). Not surprisingly, a maximum T' and a maximum $\langle Q''_{\mathrm{rad}} \rangle$ are linked. For GWs and especially TWs, $\langle Q''_{\mathrm{rad}} \rangle$ is limited at high altitudes by non-LTE.

Finally the influence of a non-isothermal background is taken into account. For this purpose, Eqs. (2.25) and (2.26) are integrated numerically. The resulting net cooling rates and the used temperature profile are shown in Fig. 2.7. For validation the analytical results of the Eqs. (2.48) and (2.49) are inserted and indicated with the subscript a.

Figure 2.7 shows a more realistic picture of the the long-wave cooling rates. The numerical solution $\langle Q_{\mathrm{rad}} \rangle$ exhibits two areas of strong cooling around the stratopause and the lower thermosphere balancing short-wave heating. The comparison with $\langle Q_{\mathrm{rad,a}} \rangle$ reveals significant wave-independent deviations due to the derivation of Eq. (2.49) for an isothermal background state. In contrast, $\langle Q''_{\mathrm{rad,a}} \rangle$ matches $\langle Q''_{\mathrm{rad}} \rangle$ pretty well for the GW and the TW with relative errors of 5 % and 1.5 %. In comparison to the isothermal atmosphere, the amount of additional net cooling has dropped by a third. This is simply caused by the fact that the isothermal reference temperature is higher between $60 - 110$ km.

A different behavior is found for $\langle Q_{\mathrm{rad}} \rangle$ for the RW. The slight temperature variations of a few Kelvins below 20 km lead to additional heating in the troposphere and in the MLT. The additional heating is caused by a wave-induced increase of upward and downward radiative energy fluxes. This once again emphasizes that U', D', U'' and D'' can not be neglected for waves with relevant amplitudes in the troposphere. In the upper stratosphere, increased thermal emission due to maximum T' is compensated by U', D', U'' and D'' and almost no additional net cooling occurs. In comparison with Fig. 2.4 the effect of wave-induced radiative energy fluxes is stronger due to higher temperatures near the Earth's surface. This is an example for non-local vertical coupling by long-wave radiation.

A point we do not have considered yet is a feedback of the additional net cooling rate on the background. Reduced additional cooling might follow. This fact is not included in Kutepov et al. [2013] and Kutepov et al. [2007] as well.

2.10 Summary

With focus on GWs and TWs it has been shown that:

- The absolute radiative fluxes remain unchanged.
- Additional cooling is noticeable and caused by increased thermal emission.
- In the temporal mean, the additional cooling reaches up to 0.7 K/day for TWs.
- Additional cooling depends on non-LTE.
- Simple analytical expressions describe the additional cooling rates adequately:

$$Q_{\mathrm{wave}} = Q'_{\mathrm{rad}} + Q''_{\mathrm{rad}} \qquad \langle Q_{\mathrm{wave}} \rangle = \langle Q''_{\mathrm{rad}} \rangle$$

$$Q'_{\mathrm{rad}} = -16\,\kappa\,\sigma\,(1-\omega_{\mathrm{s}})\,T_{\mathrm{r}}^{3}\,T' \qquad \langle Q''_{\mathrm{rad}} \rangle = -12\,\kappa\,\sigma\,(1-\omega_{\mathrm{s}})\,T_{\mathrm{r}}^{2}\,\widehat{T}'^{\,2}$$

$$Q''_{\mathrm{rad}} = -24\,\kappa\,\sigma\,(1-\omega_{\mathrm{s}})\,T_{\mathrm{r}}^{2}\,T'^{\,2}$$

3 Atmospheric waves influenced by radiation

3.1 Introduction

The starting point of describing atmospheric waves are the fluid equations of motion that follow from conservation of momentum, energy and mass. To obtain a particular wave type, scale analyses with adjusted spatial and temporal dimensions are applied to these equations. Furthermore, one has to linearize about a given basic flow. Different dominant terms remain indicating the different restoring forces for each wave type. This is commonly referred to as *linear wave theory*.

3.2 Linear theory of gravity waves

Our basis is given by the *primitive equations* on the f-plane. Applying the *anelastic approximation* and linearizing with the aforementioned perturbation ansatz $X(x, y, z, t) = X_{\mathrm{r}}(z) + X'(x, y, z, t)$, we obtain:

$$d_t\, u' - v'\, f + \frac{\partial_x\, p'}{\rho_{\mathrm{r}}} = 0\,, \tag{3.1}$$

$$d_t\, v' + u'\, f + \frac{\partial_y\, p'}{\rho_{\mathrm{r}}} = 0\,, \tag{3.2}$$

$$\partial_z \left(\frac{p'}{\rho_{\mathrm{r}}}\right) + g\, \frac{\rho'}{\rho_{\mathrm{r}}} = 0\,, \tag{3.3}$$

$$d_t\, T' + \frac{N_r^2\, T_{\mathrm{r}}}{g} w' = \frac{Q}{c_{\mathrm{p}}}\,, \tag{3.4}$$

$$\partial_x\, u' + \partial_y\, v' + (\partial_z - \frac{1}{H})\, w' = 0\,, \tag{3.5}$$

where $N_{\mathrm{r}} = \sqrt{g^2/(c_p\, T_{\mathrm{r}})}$ is the buoyancy frequency of an isothermal atmosphere, Q is diabatic heating, $f = 2\, \sin(\phi)\, \omega_{\mathrm{E}}$ the Coriolis parameter and $(u',\, v',\, w')$ is the perturbation wind vector. d_{t} stands for $(\partial_t + U\, \partial_x)$ with U being the zonal background wind. Small-scale diffusion is neglected for our purpose. The system is completed with the *Boussinesq approximation* for GWs

$$-\frac{\rho'}{\rho_{\mathrm{r}}} = \frac{T'}{T_{\mathrm{r}}}\,. \tag{3.6}$$

We require that the background atmosphere is not subject to any net heating. The wave-related diabatic heating owing to radiative cooling is (see Eq. (2.42))

$$\frac{Q}{c_\mathrm{p}} = \frac{Q'_\mathrm{rad}}{c_\mathrm{p}} = -\underbrace{\frac{16\,\kappa\,(1-\omega_\mathrm{s})\,\sigma\,T_\mathrm{r}^3}{c_\mathrm{p}}}_{=\alpha(z)}\,T'\,. \tag{3.7}$$

Q'_rad is synonymously called damping rate with the cooling rate coefficient[2] α. To find a simple dispersion relation, we restrict ourselves to one horizontal dimension (for consistency the x-axis), assume medium-frequency waves as well as $m^2 \gg \frac{1}{H^2}$ and introduce the ansatz

$$(u', w', \frac{p'}{\rho_\mathrm{r}}, T', \frac{\rho'}{\rho_\mathrm{r}})(x,z,t) = (A_{u'}, A_{w'}, A_{p'}, A_{T'}, A_{\rho'})\,\widetilde{w}(z)\,\exp\left\{i\,(k\,x-\omega\,t)+\frac{z}{2\,H}\right\}. \tag{3.8}$$

Then the linear equation system can be written as

$$\begin{pmatrix} i\,\omega_\mathrm{I} & 0 & \frac{i\,k}{\rho_\mathrm{r}} & 0 & 0 \\ 0 & 0 & (\partial_z+\frac{1}{2\,H})\widetilde{w} & 0 & g\,\widetilde{w} \\ 0 & \frac{T_\mathrm{r}\,N_\mathrm{r}^2}{g} & 0 & i\,\omega_\mathrm{I}+\alpha & 0 \\ i\,k\,(\partial_z+\frac{1}{2\,H})\widetilde{w} & (\partial_z^2-\frac{1}{4\,H^2})\widetilde{w} & 0 & 0 & 0 \\ 0 & 0 & 0 & 1/T_\mathrm{r} & 1/\rho_\mathrm{r} \end{pmatrix} \begin{pmatrix} A_{u'} \\ A_{w'} \\ A_{p'} \\ A_{T'} \\ A_{\rho'} \end{pmatrix} = 0 \tag{3.9}$$

where $\omega_\mathrm{I} = k\,(U-c)$ is the intrinsic frequency. The sign convention is $k > 0$ and $\omega_\mathrm{I} < 0$. Setting the determinate of the coefficient matrix to zero yields the relation for the nontrivial solutions

$$\underbrace{\left(\partial_z^2 - \frac{1}{4\,H^2}\right)}_{\approx\,\partial_z^2}\widetilde{w}(z) + \underbrace{\frac{N_\mathrm{r}^2\,k^2}{(\omega_\mathrm{I}^2 - i\,\alpha\,\omega_\mathrm{I})}}_{:=m^2}\,\widetilde{w}(z) = 0\,. \tag{3.10}$$

Since $1/\alpha$ is in the order of days and $1/\,|\omega_\mathrm{I}|$ of hours, terms of α^2 are omitted. Thus

$$m^2 \approx \frac{N_\mathrm{r}^2\,k^2}{(\omega_\mathrm{I} - i\,\alpha/2)^2}\,. \tag{3.11}$$

To get the final result of the dispersion relation real and imaginary parts are split

$$m = \underbrace{\frac{N_\mathrm{r}\,k}{\omega_\mathrm{I}}}_{=:\,m_\mathrm{r}} + i\,\underbrace{\frac{N_\mathrm{r}\,k\,\alpha}{2\,\omega_\mathrm{I}^2}}_{=:\,m_\mathrm{i}} = m_\mathrm{r} + i\,\frac{m_\mathrm{r}\,\alpha}{2\,\omega_\mathrm{I}}\,. \tag{3.12}$$

For $\alpha = 0$, the dispersion relation is identical to the one that is mentioned for medium-frequency GWs in Fritts and Alexander [2003]. Here, m is allowed to vary slightly with height due to the background atmosphere. A solution of Eq. (3.10) can then be found by

[2] Other authors often call it damping rate coefficient, damping rate parameter or just damping rate.

applying the WKB approximation[3]. It states that $|\partial_z m| \ll |m^2|$. Applying the ansatz $\widetilde{w}(z) = e^{\varphi(z)}$, the first order WKB solution is

$$\varphi(z) = \int_{\mathrm{z_s}}^{z} i\, m\, dz' + \frac{1}{2}\, ln \frac{m_r(z_s)}{m_r(z)}\,. \tag{3.13}$$

According to our assumption of an isothermal background state at rest, m_r is constant, hence

$$\exp\{\varphi\} = \exp\left\{\int_{\mathrm{z_s}}^{z} i\, m\, dz'\right\} = \exp\left\{i\, m_\mathrm{r} - \int_{\mathrm{z_s}}^{z} m_\mathrm{i}\, dz'\right\}\,. \tag{3.14}$$

With

$$m_i(z) = \frac{m_\mathrm{r}\,\alpha(z)}{2\,\omega_\mathrm{I}} = \frac{m_\mathrm{r}}{2\,\omega_\mathrm{I}}\,\frac{16\,\kappa\,(1-\omega_\mathrm{s}(z))\,\sigma\,T_\mathrm{r}^3}{c_\mathrm{p}}\,, \tag{3.15}$$

where $\omega_\mathrm{s}(z)$ is defined by Eq. (2.27), a wave-damping coefficient can be defined as

$$d(z) := \exp\left\{-\int_{\mathrm{z_s}}^{z} m_\mathrm{i}\, dz'\right\} = \left(\frac{\omega_\mathrm{s}(z_\mathrm{s})}{\omega_\mathrm{s}(z)}\right)^{\frac{m_\mathrm{r}\,H}{2\,\omega_\mathrm{I}}\,\frac{16\,\kappa\,\sigma\,T_\mathrm{r}^3}{c_\mathrm{p}}}\,. \tag{3.16}$$

The wave-damping coefficient d describes the ratio of damped to undamped temperature amplitudes and is limited to $0 \le d(z) \le 1$. Under perfect LTE condition ($c_{21}/A_{21} \gg 1$; see Sec. 2.4), the wave-damping coefficient becomes

$$d(z) \approx \exp\left\{-\frac{m_\mathrm{r}}{2\,\omega_\mathrm{I}}\,\frac{16\,\kappa\,\sigma\,T_\mathrm{r}^3}{c_\mathrm{p}}\,(z - z_\mathrm{s})\right\}\,, \tag{3.17}$$

whereas from total non-LTE condition ($c_{21}/A_{21} \ll 1$) follows that $d \approx 1$. The final result of the radiatively-damped temperature perturbation reads

$$T' = A_{T'}\, d(z)\, \exp\left\{i\,(k\,x - \omega\,t) + (i\,m_\mathrm{r} + \frac{1}{2\,H})\,z\right\}\,. \tag{3.18}$$

3.3 Impact of long-wave radiation on gravity wave dynamics

The amount of damping depends on the wave properties (m_r and ω_I) as well as on the background state of the atmosphere due to the cooling rate coefficient. It would be recommendable to consider a realistic T_r in Eq. (3.14) because of T_r^3 in α. But in this case an analytical formula can not be derived.

$d(z)$ is depicted for different values of k, ω_I and T_r in Fig. 3.1. It shows that amplitude damping increases with height. This corresponds to a permanent loss of wave energy to the radiation field. Above 100 km, radiative damping is limited by non-LTE. In case of shorter vertical wavelengths the damping becomes generally stronger (see blue and black line for $m_\mathrm{r} = 3.6$/km versus the red and green one for $m_\mathrm{r} = 1.8$/km) because of

[3] Refers to the method of approximating solutions to linear, second-order differential equations that was developed by Wentzel, Kramers, and Brillouin.

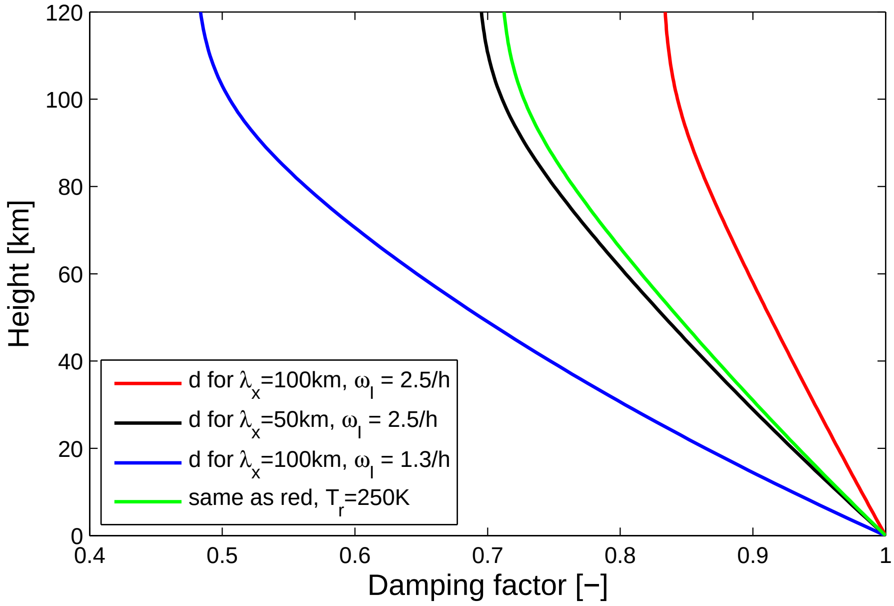

Figure 3.1: The wave-damping coefficient $d(z)$ depending on wave properties and the background atmosphere. If the red line states a reference wave at $T_\mathrm{r} = 245$ K, blue has half intrinsic frequency, black half horizontal wavelength and green line 5 K higher T_r.

the dependence of exponential damping in Eq. (3.16) on $m_\mathrm{r}/\omega_\mathrm{I}$. The physical reason for this behavior can be understood when considering the group velocity $c_{g,z}$

$$|c_{g,z}| = \left|\frac{\partial\omega_\mathrm{I}}{\partial m_\mathrm{r}}\right| = \left|\frac{\omega_\mathrm{I}}{m_\mathrm{r}}\right| . \tag{3.19}$$

It can be seen that strong damping is related to slow vertical propagation of the wave. In this case, the wave is longer subject to energy loss by radiation. To emphasize this physical issue, $d(z)$ can be reformulated. We define the time scale for the radiative cooling as $\tau_\mathrm{rc} = 2/\alpha$ and the residence time of the GW in the atmosphere as $\tau_{res} = \Delta z/|c_{ph,z}|$ with Δz being the vertical distance between the source and the breaking region. Neglecting non-LTE, the wave-damping coefficient can be expressed as

$$d = \exp\left\{-\frac{m_\mathrm{r}\,\alpha}{2\,\omega_\mathrm{I}}\,(z - z_s)\right\} =: \exp\left\{-\frac{\Delta z}{\tau_\mathrm{rc}\,c_{\mathrm{g},z}}\right\} = \exp\left\{-\frac{\tau_\mathrm{res}}{\tau_\mathrm{rc}}\right\} . \tag{3.20}$$

Figure 3.1 shows that a slight increase of T_r by 2% is followed by a strong nonlinear additional damping of the amplitude by 20%.

As a final comment, the damping of GWs is expected to be highly variable due to the variety of wave residence times and background states. Therefore, a sophisticated statistical gravity-wave model or GCM simulations with resolved GWs is needed to make general statements of the effect of radiative damping on GWs.

3.4 Linear theory of tidal waves

The version of KMCM used in this study has a horizontal resolution of T32 (grid resolution around the equator of 420×420 km). GWs are barely resolved (min. resolved $\lambda_x = 1260$ km). This restriction does not affect atmospheric tides, which have planetary scales. Some numerical tests revealed that especially tides in the MLT show significant interactions with long-wave radiation. We shall therefore investigate both damping of the tides and additional cooling by these waves. In the future, an extension to GWs could be done by using a high spatial resolution to explicitly simulate GWs. To support the analysis of results gained with KMCM for tides, a theoretical treatment is provided first. This follows the text of Lindzen and Chapman [1969]; hereinafter referred to as LC.

"Atmospheric tides refer to those oscillations in the atmosphere whose periods are integral fractions of a lunar or solar day" [Lindzen, 1979]. The basic equations of the classical tidal theory are nearly the same as mentioned for GWs, compare Eqs. (3.1) - (3.5) with LC (p. 113, Eqs. (8) - (13)[4]). The most significant difference is an extension from a f-plane in Cartesian coordinates to spherical coordinates and relaxing the Boussinesq approximation for GWs. In general, tidal waves can be considered as forced gravity waves with planetary scales.

Tidal wave theory deals with fields that are periodically in time and longitude. As a first step it is assumed that

$$f(\lambda, \phi, z, t) = f^{\omega,s}(\phi, z)\, e^{i(\omega t + s\lambda)}\,, \tag{3.21}$$

with λ being the longitude, ϕ the latitude, ω the tidal angular frequency and s the zonal wavenumber. The set of differential equations can now be combined to form one partial differential equation with respect to ϕ and z. A solution is found by the method of separation of variables giving an ordinary differential equation for ϕ and another one for z. The constant of separation is $h_n^{\omega,s}$ and is called *equivalent depth* [5].

The latitude problem

$$F(\Theta_n^{\omega,s}) = -\frac{4\,a^2\,\omega_{\mathrm{E}}^2}{g\,h_n^{\omega,s}}\,\Theta_n^{\omega,s}\,, \quad \Theta_n^{\omega,s} = \Theta_n^{\omega,s}(\phi) \tag{3.22}$$

is the well-known *Laplace's Tidal Equation.* Here, F is a linear operator, a the Earth's radius and ω_{E} the Earth's angular frequency. Eq. (3.22) is an eigenfunction-eigenvalue problem. The eigenfunctions $\Theta_n^{\omega,s}$ are called *Hough Functions* after Hough who pioneered in the solution of Eq. (3.22) in the late 19th century. The Hough functions can be expressed as an infinite sum of *associated Legendre polynomials.*

The altitude problem is often called the *vertical structure equation.* In LC, $T_{\mathrm{r}} = T_{\mathrm{r}}(z)$. We set $T_{\mathrm{r}} = const.$ To include infrared cooling, the same approach as done for GWs,

[4] For quantities differently denoted in LC, the letters are changed to those used in this work before. Sign conventions are preserved.

[5] In context with the historical problem the same constant corresponds to the depth of ocean.

i.e. $Q'_{\mathrm{rad}}/c_{\mathrm{p}} = \alpha(z)\,T'$, is incorporated in the thermodynamic equation (see LC, p. 165, Eqs. (193) - (196)). The thermal excitation of tides is assumed to be located at altitudes below such that a free wave equation can be considered. The vertical structure equation can then be written as

$$\partial_z^2\,\gamma_n^{\omega,s} + \underbrace{\left(\frac{\kappa_{\mathrm{ig}}}{h_n^{\omega,s}\,H}\left(1+\frac{\alpha}{i\,\omega}\right)^{-1} - \frac{1}{4\,H^2}\right)}_{:=m^2}\gamma_n^{\omega,s} = 0\,, \tag{3.23}$$

where $\kappa_{\mathrm{ig}} = 2/7$. Using $\omega^2 \gg \alpha^2$, m is approximately given by

$$m \approx \underbrace{\sqrt{\frac{\kappa_{\mathrm{ig}}}{h_n^{\omega,s}\,H} - \frac{1}{4\,H^2}}}_{=:m_{\mathrm{r}}} + i\,\underbrace{\frac{\alpha}{2\omega}\,\frac{\frac{\kappa_{\mathrm{ig}}}{h_n^{\omega,s}\,H}}{\sqrt{\frac{\kappa_{\mathrm{ig}}}{h_n^{\omega,s}\,H} - \frac{1}{4\,H^2}}}}_{m_{\mathrm{i}}}\,, \tag{3.24}$$

$$= m_{\mathrm{r}} + i\,\frac{m_{\mathrm{r}}^2 + \frac{1}{4\,H^2}}{m_{\mathrm{r}}}\,\frac{\alpha}{2\,\omega}\,. \tag{3.25}$$

Except for the term $\frac{1}{4\,H^2}$, Eq. (3.25) is equivalent to Eq. (3.12). Also, the WKB ansatz yields a result that is analogous to the previous one for GWs.

$$\gamma_n^{\omega,s} = \gamma_{n,0}^{\omega,s}\,\exp\left\{\int_{z_{\mathrm{s}}}^{z} i\,m\,dz'\right\}\,, \tag{3.26}$$

$$= \gamma_{n,0}^{\omega,s}\,\underbrace{\left(\frac{\omega_{\mathrm{s}}(z_{\mathrm{s}})}{\omega_{\mathrm{s}}(z)}\right)^{\frac{m_{\mathrm{r}}^2+\frac{1}{4\,H^2}}{m_{\mathrm{r}}}\,\frac{H}{2\,\omega}\,\frac{16\,\kappa\,\sigma\,T_{\mathrm{r}}^3}{c_{\mathrm{p}}}}}_{=:d(z)}\,e^{i\,m_{\mathrm{r}}\,z}\,. \tag{3.27}$$

The overall solution for the temperature variations due to tides is

$$T'(\lambda,\theta,z,t) = \sum_{\omega,s,n} e^{i(\omega t + s\lambda)}\,\Theta_n^{\omega,s}\,T_n'^{\,\omega,\mathrm{s}}\,, \tag{3.28}$$

where the radiatively-damped amplitude reads

$$T_n'^{\,\omega,\mathrm{s}} = -\left(1+\frac{\alpha}{i\,\omega}\right)^{-1}\frac{(\gamma-1)\,T_{\mathrm{r}}}{i\,\omega}\,\gamma_n^{\omega,s}e^{z/2H}\,. \tag{3.29}$$

3.5 Impact of long-wave radiation on thermal tides

Eq. (3.24) states that vertical propagation and radiative damping of tides depend on $h_n^{\omega,s}$. To estimate effects excited by and exerted on tides, it is necessary to know the relevant $h_n^{\omega,s}$ in the middle atmosphere. In principle, there is an infinite number of Hough functions (and equivalent depths), but only a few will project on a specific excitation

ω [ω_{E}], s n	2,2 2	2,2 4	2,2 6	1,1 1	1,1 3	1,1 -2	1,1 -4
$h_n^{\omega,s}$ [km]	7.85	2.11	0.96	0.69	0.12	-12	-1.7
m_{r} [1/km]	0.015	0.12	0.19	0.23	0.57	0.09 i	0.17 i
λ_z [km]	433	53	33	27	11	-	-
symmetric	yes	yes	yes	yes	yes	yes	yes
vertical propagation	yes	yes	yes	yes	yes	no	no

Table 3.1: Characteristics of the most important symmetric Hough modes calculated for an isothermal background state $T_{\mathrm{r}} = 245$ K. As LC noted, for a realistic temperature profile vertical propagation of the semidiurnal mode $n = 2$ is only possible below the mesosphere.

mechanism. Since the set of all Hough functions $\{\Theta_n^{\omega,s}\}$ is complete, any given excitation function $Q^{\omega,s}$ can be expanded as

$$Q^{\omega,s} = \sum_n Q_n^{\omega,s}(z)\,\Theta_n^{\omega,s}(\theta)\,, \tag{3.30}$$

what allows for the identification of relevant Hough functions. LC pointed out that absorption of solar insolation is the dominant excitation mechanism. The main contributions are absorption by water vapor in $0-12$ km and absorption by ozone between $20-80$ km height (centered around 45 km) [Forbes, 1984]. In addition, the diurnal variation of moist convection in the tropical convergence zones contributes to the generation of tides. Tides responding to these excitations are called thermal tides, hereinafter just referred to as “tides”. Tides are divided into migrating (following the apparent motion of the Sun) and non-migrating tides (faster/slower westward propagation compared to the Sun’s motion, eastward propagation or steady-state oscillations). Migrating tides are of greater importance throughout the middle atmosphere [Forbes, 1984; Hagan et al., 1997]. Therefore, non-migrating tides will not be further considered in the present study.

The Hough functions that match best with the thermal excitation are the migrating diurnal ones $\Theta_n^{\omega_{\mathrm{E}},1}$, meaning $\omega = \omega_{\mathrm{E}}$ and $s = 1$. Hough functions of the migrating diurnal tide[6] with positive equivalent depths (sometimes called internal or gravitational modes) are $\Theta_1^{\omega_{\mathrm{E}},1}$, $\Theta_2^{\omega_{\mathrm{E}},1}$, $\Theta_3^{\omega_{\mathrm{E}},1}$, ... whereas negative equivalent depths (external or rotational modes) are denoted as $\Theta_{-1}^{\omega_{\mathrm{E}},1}$, $\Theta_{-2}^{\omega_{\mathrm{E}},1}$, $\Theta_{-3}^{\omega_{\mathrm{E}},1}$, ... A positive odd or a negative even n indicates a Hough function that is symmetric about the equator. All other n are antisymmetric Hough functions. The thermal excitation of the migrating semidiurnal tide, $\omega = 2\,\omega_{\mathrm{E}}$ and $s = 2$, is only a fraction of the diurnal tidal excitation. Nevertheless, the migrating semidiurnal tide is of similar importance as the diurnal tide throughout the atmosphere. There exist only solutions with positive $h_n^{2\omega,2}$. Semidiurnal Hough

[6]The term ”migrating diurnal tide“ refers to the complete temperature field that is given by Eq. (3.28) as a sum over n for $\omega = \omega_{\mathrm{E}}$ and $s = 1$. A ”migrating diurnal Hough mode“ is the temperature field defined by Eq. (3.28) for a particular n and $\omega = \omega_{\mathrm{E}}$ and $s = 1$.

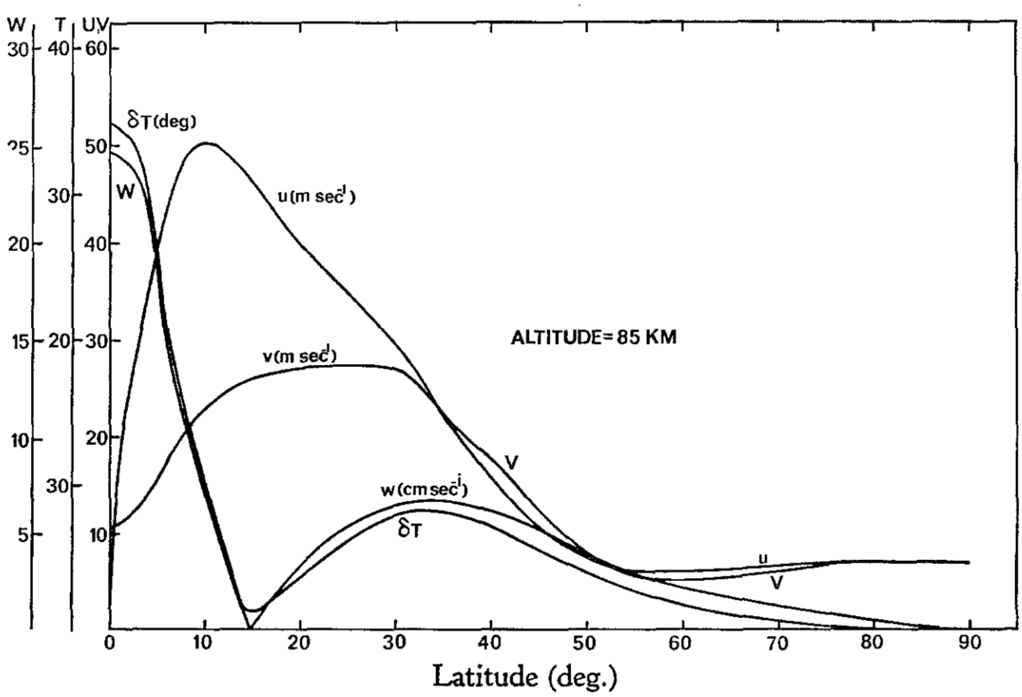

Figure 3.2: Latitudinal distribution of the amplitudes of the migrating diurnal components of the u', v', w' and T' fields at 85 km excited by the absorption of solar insolation by water vapor and ozone for equinoctial conditions. (From Lindzen [1967], u - northerly velocity and v - westerly velocity.)

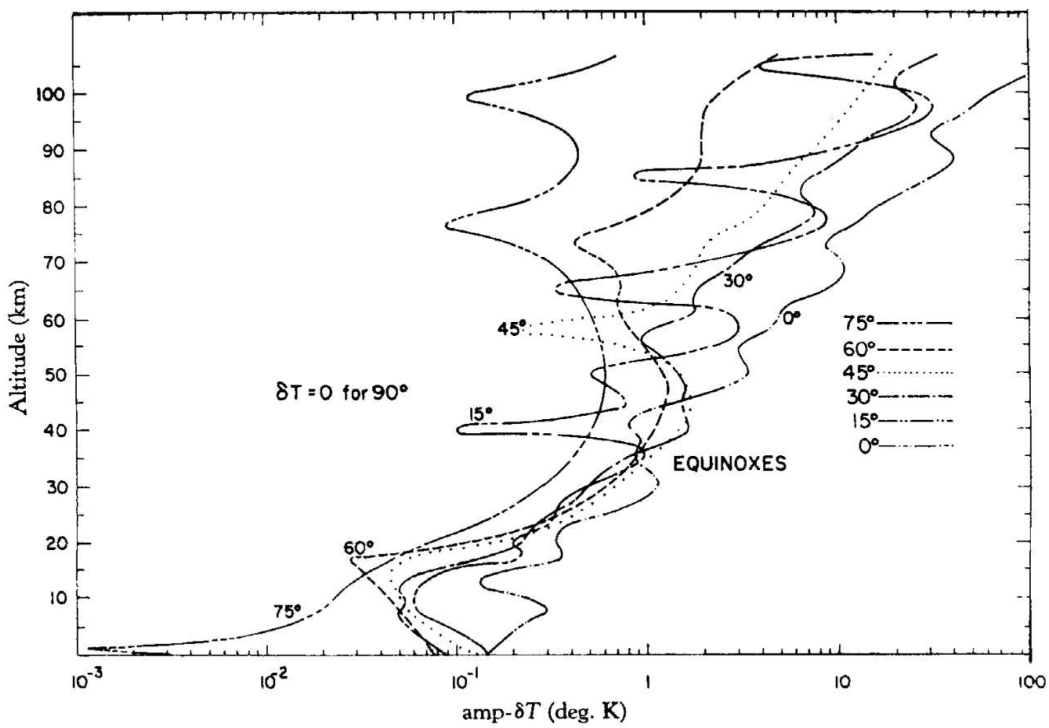

Figure 3.3: Vertical profile of the temperature amplitude of the migrating diurnal tide for different latitudes under same conditions as in Fig 3.2. (From Lindzen [1967])

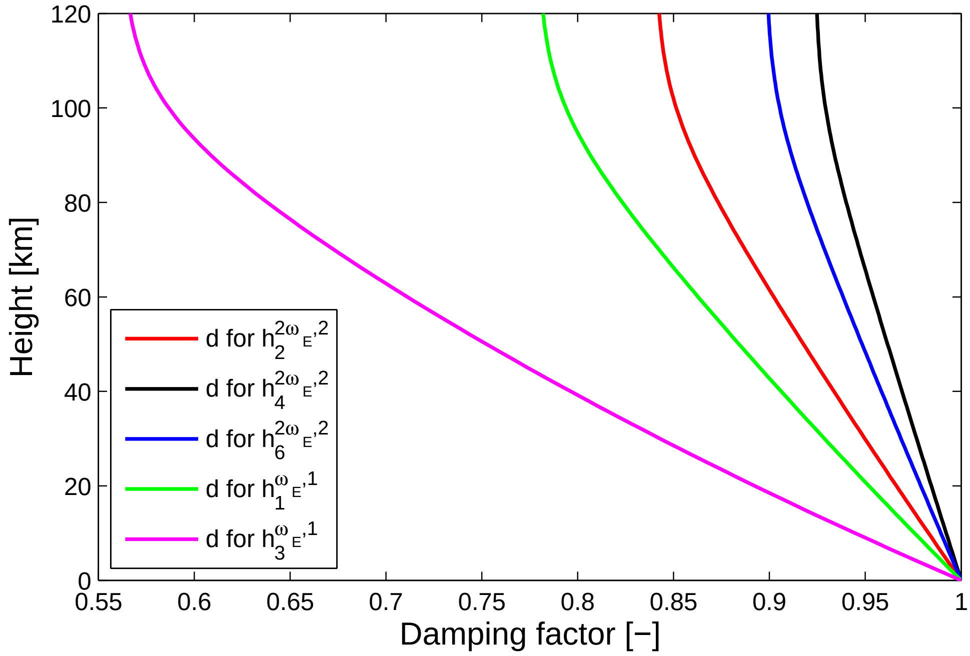

Figure 3.4: The wave-damping coefficient $d(z)$, which corresponds to the ratio of damped to undamped amplitude, for different Hough modes and equivalent depths for $T_\mathrm{r} = 245$ K. With the exception of $\Theta_2^{2\omega_\mathrm{E},2}$, higher order modes (increasing n) are damped more efficiently.

functions $\Theta_1^{2\omega_\mathrm{E},2}$, $\Theta_2^{2\omega_\mathrm{E},2}$, $\Theta_3^{2\omega_\mathrm{E},2}$, ... with even (odd) n are symmetric (antisymmetric) about the equator. It is reasonable that symmetric Hough functions are more important because they receive the bulk excitation due to the approximately latitudinal symmetry of solar insolation (see Eq. (3.30)). Table 3.1 provides an overview of the most important Hough modes and some of their basic properties.

From tidal excitation and propagation it is expected that, in general, amplitudes of all modes vary with latitude, altitude and season. A detailed overview can be found e.g. in LC, Lindzen [1979] or Forbes [1984]. But some important features, we shall address later, are

- The mode $\Theta_2^{2\omega_\mathrm{E},2}$ dominates the migrating semidiurnal tide throughout the atmosphere except for the MLT. Its large equivalent depth in combination with decreasing temperature in the mesosphere leads to exponential decay with altitude in the MLT.

- The mode $\Theta_4^{2\omega_\mathrm{E},2}$ mainly contributes to the migrating semidiurnal tide in the lower thermosphere [Hong and Lindzen, 1976].

- No vertical propagation is possible for diurnal modes with negative equivalent depth, because imaginary m_r means trapping (see Eq. (3.24)) to the excitation region. Therefore, the modes $\Theta_1^{\omega_\mathrm{E},1}$, $\Theta_3^{\omega_\mathrm{E},1}$ and $\Theta_5^{\omega_\mathrm{E},1}$ are the main diurnal tidal components in the MLT.

- Vertical propagation of the migrating diurnal tide is limited to the tropics and subtropics. The reason is that the tidal frequency ω must be larger than the Coriolis parameter (extrapolating from linear theory of GW). This condition is fulfilled for $f(0°) = 0 \leq f \leq f(30°) = 1\,\omega_\mathrm{E}$.

- The latitudinal temperature structure of a mode is directly connected to the Hough funtion (see Eq. (3.29)).

- Amplitudes of vertical propagating tides grow with altitude by the factor $e^{z/2H}$ as long as refraction by the mean wind and vertical variations of the background temperature are neglected.

Summarizing, the strongest T' can be expected in the MLT due to the migrating diurnal tide in a latitude band between $-30°$ to $30°$ for equinoctial conditions. This is also evident from Figs. 3.2 and 3.3.

We now turn to the wave-damping coefficient depending on the equivalent depth of each Hough mode. For different Hough modes, $d(z)$ is shown in Fig. 3.4. A physical explanation of the findings of Fig. 3.4 can be given when considering again the group velocity. There is no dispersion relation for tides due to the discrete wave spectrum. LC assumed the group velocity of GWs also being applicable to tides. Due to the planetary scales of tides, the extended dispersion relation of GWs

$$m_\mathrm{r} = \sqrt{\frac{N_\mathrm{r}^2\,k^2}{\omega_\mathrm{I}^2} - \frac{1}{4\,H^2}}\,, \tag{3.31}$$

is used for the derivation of the group velocity

$$|c_{g,z}| = \left|\frac{\partial \omega}{\partial m_\mathrm{r}}\right| = \left|\frac{m_\mathrm{r}\,\omega}{m_\mathrm{r}^2 + \frac{1}{4\,H^2}}\right|\,. \tag{3.32}$$

The approximation $m_\mathrm{r}^2 \gg \frac{1}{4\,H^2}$ applies for most Hough modes that are symmetric about the equator. In this case, it follows from Eqs. (3.24) and (3.32) that modes with a smaller equivalent depth show a lower $|c_{g,z}|$ and are damped more efficiently by long-wave radiation. This assumption can not be made for the Hough mode $\Theta_2^{2\omega_\mathrm{E},2}$. For $T_\mathrm{r} = 245$ K, the vertical wavelength of $\Theta_2^{2\omega_\mathrm{E},2}$ approaches zero. In such a case the group velocity would tend to zero and radiative damping would get infinitely strong.

3.6 Summary

- Radiative damping can be included in the linear theory of GWs and TWs in WKB approximation.
- For medium-frequency GWs and thermal TWs the wave-damping coefficient is

$$d = \exp\left\{ -\int_{z_\mathrm{s}}^{z} \frac{m_\mathrm{r}^2 + \frac{1}{4\,H^2}}{m_\mathrm{r}} \, \frac{\alpha}{2\,\omega} \, dz' \right\} .$$

- The amount of radiative damping depends on the cooling rate coefficient α and the residence time of the wave in the atmosphere.

4 Interaction of atmospheric waves and thermal radiation in a mechanistic GCM

4.1 Motivation and Introduction

Using a GCM offers the possibility to determine wave-radiation interaction for a realistic background atmosphere and reasonable dynamics of resolved waves. Furthermore, several approximations can be avoided that have been made in our semi-analytical calculations.

In this chapter, estimates of TW-induced cooling rates and radiative damping of TWs using KMCM simulations are presented and interpreted with respect to the previous chapters.

First of all, the basic properties of KMCM are mentioned, followed by some information about the implemented radiative transfer scheme. As a basis for our analysis, we continue with a presentation of background temperatures and the resolved wave activity in KMCM. Afterward, it is shown how additional cooling rates and cooling rate coefficients can be derived from KMCM simulations. An extrapolation of these results to additional radiative net cooling rates by GWs is proposed.

Radiative damping of tides will be addressed by a comparison of model runs where the thermal radiation does or does not interact with waves. Radiative damping on the migrating diurnal and the semidiurnal tide will be considered separately.

4.2 KMCM in a nutshell

KMCM (Kühlungsborn Mechanistic general Circulation Model) is a mechanistic general circulation model. The dynamical core solves the primitive equations by using the following numerical schemes.

- A vertical discretization with a terrain following vertical hybrid coordinate, according to Simmons and Burridge [1981] is applied.
- The horizontal representation makes use of the spectral transform method as introduced by Machenhauer and Rasmussen [1972].
- Time integration is done by the semi-implicit leapfrog scheme following Asselin [1972] and Hoskins and Simmons [1975].

The prognostic variables are the horizontal vorticity, horizontal divergence, temperature, surface pressure, surface temperature and specific humidity. The latter is treated as a tracer and allows to explicitly incorporate an idealized tropospheric moisture cycle. The model resolution is triangular spectral truncation at wavenumber 32 (T32) with 70 vertical full levels reaching up to $\approx$ 120 km height. Important parameterizations include the non-resolved effects of horizontal and vertical diffusion of momentum and sensible heat according to Becker and Burkhardt [2007]; Becker [2003], non-orographic gravity waves following Becker and McLandress [2009] and orographic gravity waves due to Wolf [2013]. The radiative transfer is described in Knöpfel and Becker [2011].

4.3 Radiative transfer scheme in KMCM

The long-wave radiative transfer scheme of KMCM is idealized when compared to state-of-the-art schemes. The simplifications of this scheme, e.g. the restriction to only four frequency bands, allow for high computational efficiency. For example, the radiative transfer is evaluated for every model time step. This is required in order to investigate the interaction of resolved atmospheric waves with long-wave radiation.

The scheme is based on Eddington-type RTEs for U and D. Important features that are not incorporated into the radiative transfer model from Chap. 2 are:

- finite frequency bands (k): (1) O_3 9.6 μm, (2) and (3) H_2O 6.3 μm and $\lambda > 5\,\mu$m, and (4) CO_2 15 μm
- mass absorber mixing ratios ρ_a^k/ρ for O_3, H_2O, and CO_2
- deviations from the gray limit parameterized using the representation of *Elsasser band model*
- improved Non-LTE parameterization due to the consideration of the efficient collisions of atomic oxygen with CO_2 in the lower thermosphere

According to these improvements the long-wave cooling rate is given by

$$Q_{\mathrm{rad}} = \sum_k 2\,\overline{\kappa}^k\,(1-\overline{\omega}_{\mathrm{s}}^k)\,(U_{\mathrm{tot}}^k + D_{\mathrm{tot}}^k - 2\,B^k)\,, \tag{4.1}$$

with k running over the four aforementioned absorber bands and overlines indicating a frequency average for each band. Furthermore, the following dependencies are incorporated: $\overline{\omega}_{\mathrm{s}}^k = \overline{\omega}_{\mathrm{s}}^k(T,\rho)$ and $\overline{\kappa}^k = \overline{K}^k\,\rho_a^k/\rho$. U_{tot}^k (D_{tot}^k) is the total upward (downward) energy flux including a covariance term due to deviations from the gray limit. Hence, our model equation (2.24) can be regarded as a simplified version of Eq. (4.1).

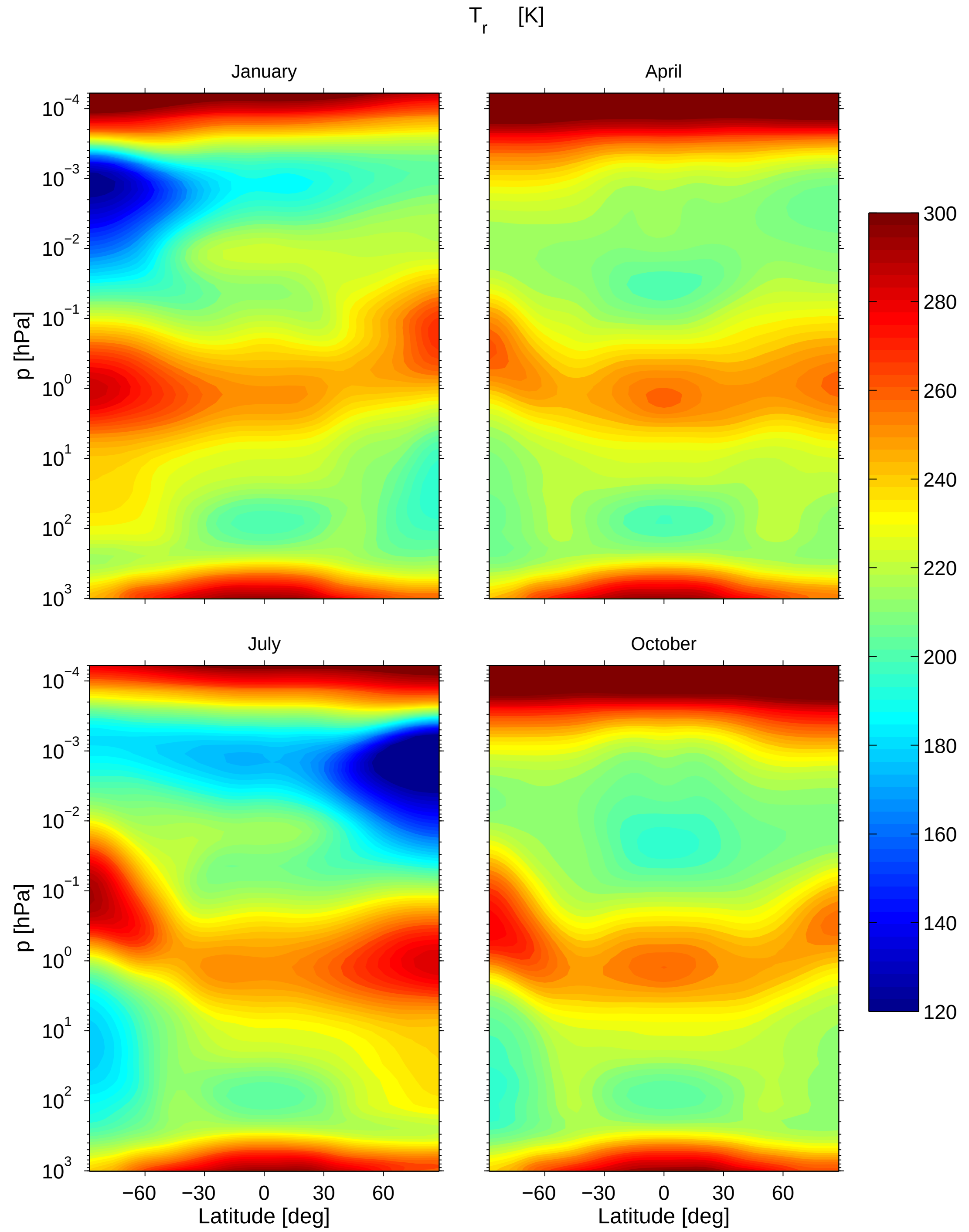

Figure 4.1: Zonally and temporally averaged temperature T_r as a function of latitude and altitude for different seasons obtained from KMCM simulations.

4.4 Background temperature and temperature perturbations in KMCM

For KMCM simulations we define the temperature of the background state by

$$T_{\mathrm{r}} = \langle [T] \rangle . \tag{4.2}$$

A zonal ($0 \leq \lambda \leq 2\pi$) and temporal ($0 \leq t \leq 10$ day) average of T is applied. As a consequence, temperature perturbations are given by

$$T' = T - T_{\mathrm{r}} \, . \tag{4.3}$$

Thus, T' represents all resolved wave deviations from the zonal mean state, subject to slow seasonal variations. Traveling waves in the MLT, especially tides, are expected to be reasonably captured. But also quasi-stationary temperature variations are included, e.g. the Siberian High in the northern hemisphere winter.

As a statistical measure the standard deviation σ_T is used

$$\sigma_T = \sqrt{\langle [(T - T_{\mathrm{r}})^2] \rangle} = \sqrt{\langle [T'^2] \rangle} \, , \tag{4.4}$$

which is identical to T'_{rms}, the root mean square of T', and related to $\widehat{T'}$, the often quoted total amplitude of T', by

$$\sigma_T = T'_{\mathrm{rms}} = \frac{\widehat{T'}}{\sqrt{2}} \, . \tag{4.5}$$

Seasonal variations of all considered quantities are evaluated by applying the aforementioned zonal and temporal average to the first 10 days of January, April, July and October. In addition, the zonal and temporal average for each month is calculated five times (five model years) and averaged. Hereafter, all calculations of standard deviations follow this method.

We start with an overview of the fields T_{r} and σ_T. In Fig. 4.1 the background temperature T_{r} is depicted as a function of latitude and altitude for different seasons. The main aspects of the atmospheric temperature distribution, like the cold summer mesopause and the warm winter stratopause, are reproduced.

Fig. 4.2 shows σ_T and reveals the resolved wave-induced temperature perturbations. In the winter hemisphere RWs appear poleward of $\phi = \pm 30°$ with maximum amplitudes around 1 and 0.1 hPa. In the southern hemisphere, the two RW-induced maxima are clearly separated. The reason is that the upper RWs are excited in situ from baroclinic instabilities (strong horizontal temperature gradients) and the lower ones are forced RWs which propagate upward from the troposphere; for comparison see McLandress et al. [2006]. In the summer hemisphere, RWs poleward of $\phi = \pm 30°$ can be found too, but they occur above the cold mesopause region. They are also generated by baroclinic instabilities. Throughout the MLT the most significant temperature perturbations are

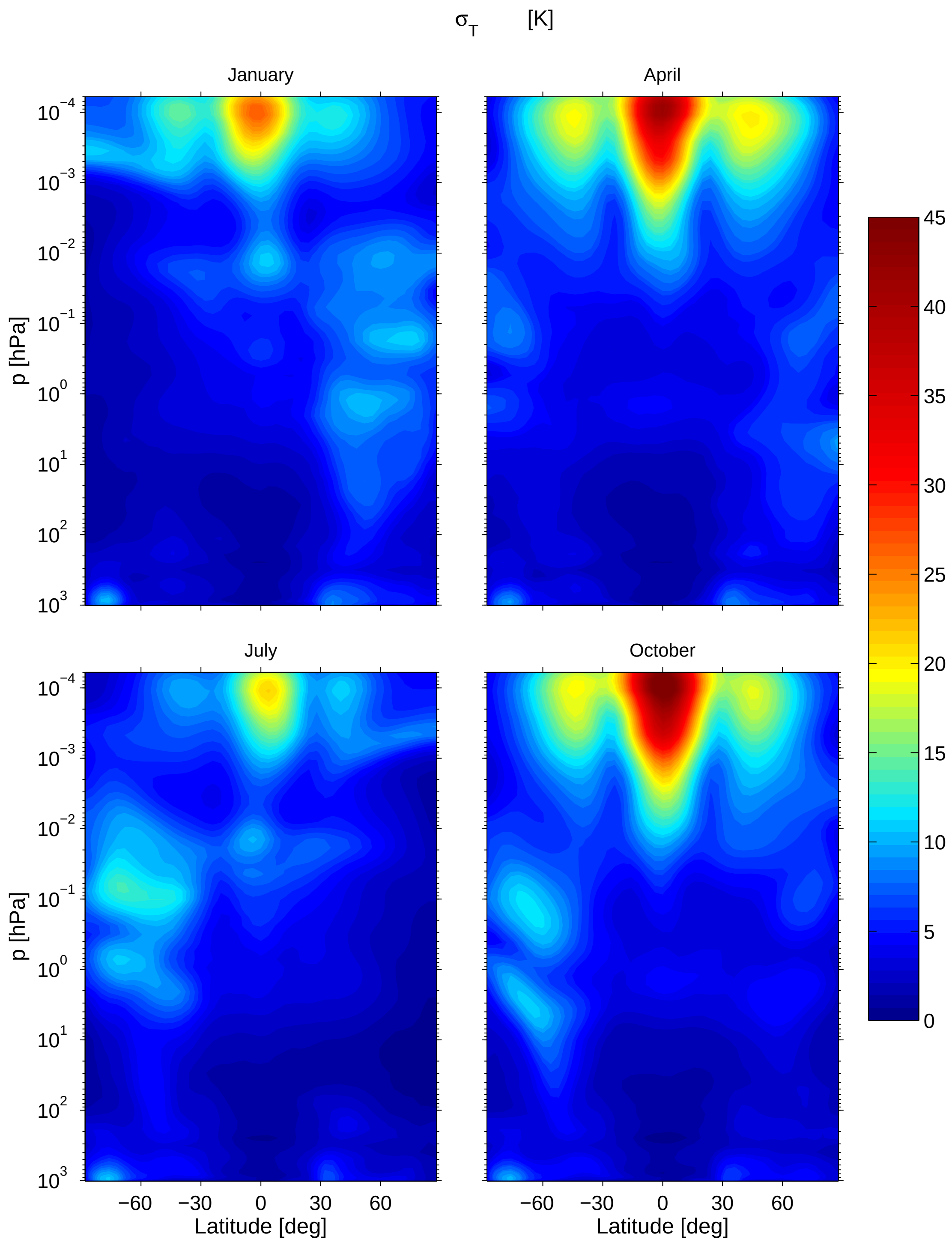

Figure 4.2: Same as Fig. 4.1, but for the standard deviation of the temperature (see Eq. (4.4)).

caused by TWs which are maximum equatorward of $\phi = \pm 30°$ around 0.0001 hPa during equinox. The secondary maxima are located at $\phi = \pm 45°$ at the same altitude and time. The latitudinal structure of tidal temperature perturbations is roughly conserved over the year. The TWs amplitudes reach values up to 65 K. A more detailed description, where also single Hough functions are considered, is given in Sec. 4.8.3.

4.5 Extracting additional cooling rates from KMCM

In principle, there are two ways of extracting the additional cooling rates from the numerical simulation. On the one hand, one could directly take the standard deviation of Q_{rad} or one could calculate the net additional cooling directly using

$$\langle [\Delta Q_{\mathrm{rad}}] \rangle = \left\langle [Q_{\mathrm{rad}}(T_{\mathrm{r}} + T')] \right\rangle - \langle [Q_{\mathrm{rad}}(T_{\mathrm{r}})] \rangle \ . \tag{4.6}$$

On the other hand, one can assume a specific dependency of $Q_{\mathrm{rad}}(T_{\mathrm{r}} + T')$ and estimate the unknown prefactors by a curve fitting procedure. This method is chosen, because we want to apply the analytical models of the previous chapters. With an appropriate fit the results of both methods are expected to be equal.

4.5.1 Curve fitting of the cooling rate

For interpreting the additional cooling rates in KMCM, $Q_{\mathrm{rad}}(T_{\mathrm{r}} + T')$ can be considered as data from a numerical experiment underlying an unknown dependency on T' that can be described using a curve fitting procedure. The actual dependency is constrained by Eq. (4.1). Thus, Eq. (4.1) is now discussed in more detail.

First, wave variations of U_{tot} and D_{tot} in Eq. (4.1) produced in the stratosphere and further above can be neglected according to the conclusion made in Sec. 2.7.

Second, Eq. (4.1) has some pressure, density and temperature dependent prefactors. Variations on these prefactors due to wave perturbations (e.g. in temperature) can cause additional wave-induced cooling rates. For large impacts of these prefactors on the cooling rate, our results from Chap. 2 would be inappropriate for describing results obtained with KMCM. Studies of these prefactors in KMCM reveal an effect of T' on $\overline{\varpi}_{\mathrm{s}}^4$ only, i.e., on the scattering albedo in the CO_2 15μm band. The variation of $\overline{\varpi}_{\mathrm{s}}^4$ occurs only for strong tidal wave activity around the equator with maximum variations of up to 10% around an altitude of 100 km. In comparison with the strong non-linearity of the Planck function this should be a minor effect that can be neglected. Using a *Taylor expansion* of $B^k(T)$ about T_{r}

$$B^k(T) = B^k(T_{\mathrm{r}}) + B_1^k(T_{\mathrm{r}})\, T' + B_2^k(T_{\mathrm{r}})\, T'^2 + \cdots \ , \tag{4.7}$$

we can write the cooling rate in the middle atmosphere with respect to the radiation scheme in KMCM as

$$
\begin{aligned}
Q_{\mathrm{rad}} \approx & \underbrace{\sum_k 2\,\overline{\kappa}_{\mathrm{r}}^k\,(1-\overline{\varpi}_{\mathrm{s,r}}^k)\,(U_{\mathrm{tot,r}}^k + D_{\mathrm{tot,r}}^k - 2\,B^k(T_{\mathrm{r}}))}_{=Q_{\mathrm{rad,r}}} + \underbrace{\sum_k -2\,\overline{\kappa}_{\mathrm{r}}^k\,(1-\overline{\varpi}_{\mathrm{s,r}}^k)\,B_1^k\,T'}_{=Q'_{\mathrm{rad}}} \\
& + \underbrace{\sum_k -2\,\overline{\kappa}_{\mathrm{r}}^k\,(1-\overline{\varpi}_{\mathrm{s,r}}^k)\,B_2^k\,T'^{\,2}}_{=Q''_{\mathrm{rad}}} + \cdots \quad .
\end{aligned} \tag{4.8}
$$

$Q_{\mathrm{rad,r}}$, Q'_{rad} and Q''_{rad} denote again the cooling rate due to the background and first- and second-order wave perturbations.

Third, the prefactors $\overline{\varpi}_{\mathrm{s}}^k$ and $\overline{\kappa}^k$ show no relevant longitudinal or temporal ($t < 10$ days) dependencies but they vary with altitude and latitude.

Taking advantage of the last point, considering time scales shorter than 10 days and assuming that $U_{\mathrm{tot}} = U_{\mathrm{tot}}(\phi, z)$ and $D_{\mathrm{tot}} = D_{\mathrm{tot}}(\phi, z)$, we can write

$$
Q_{\mathrm{rad}}(\lambda, \phi, z, t) \approx\; Q_{\mathrm{rad,r}}(\phi, z) + Q'_{\mathrm{rad}}(\lambda, \phi, z, t) + Q''_{\mathrm{rad}}(\lambda, \phi, z, t)\,. \tag{4.9}
$$

Therefore, our model function for the curve fitting is a polynomial of second order,

$$
Q_{\mathrm{rad}}(\lambda, \phi, z, t) \approx\; P_2 =\; a_0(\phi, z) + a_1(\phi, z)\,T'(\lambda, \phi, z, t) + a_2(\phi, z)\,T'^{\,2}(\lambda, \phi, z, t)\,, \tag{4.10}
$$

with latitudinal- and height-dependent fit parameters a_0, a_1 and a_2. The fitting process is carried out for the data set $[Q_{\mathrm{rad}};\, T'](\lambda, t)$ and is performed for the whole latitude and altitude domain. The fitting process is based on the *method of least squares*. An example how such a fit looks like is given in Fig. A.2 in the appendix.

The measure how well the model function fits the data of KMCM is given by the coefficient of determination

$$
R^2 = 1 - \frac{\sum\limits_{\lambda,t} (Q_{\mathrm{rad}} - P_2)^2}{\sum\limits_{\lambda,t} (Q_{\mathrm{rad}} - \overline{Q_{\mathrm{rad}}})^2}\,, \tag{4.11}
$$

running from $R^2 = 0$ (no correlation found) to $R^2 = 1$ (perfect agreement). The coefficient of determination R^2 is shown in Fig. 4.3 and confirms our previous assumptions. A description of the cooling rate with a model function of the form P_2 is very good with $R^2 > 0.95$ in the upper stratosphere and the MLT over the whole year. An exception has to be made for the summer mesopause region poleward of $\phi = \pm 60°$.

In general, it can be stated that low wave activity (vanishing σ_T), low background temperatures and high perturbations of U_{tot} in the troposphere account for small R^2. In the polar summer mesosphere all these aspects are valid and, therefore, large deviations are observed. In this case, long-wave emission is reduced and absorption of U_{tot} dominates the cooling rate. Figure 4.4 illustrates that wave-induced variations of U_{tot}

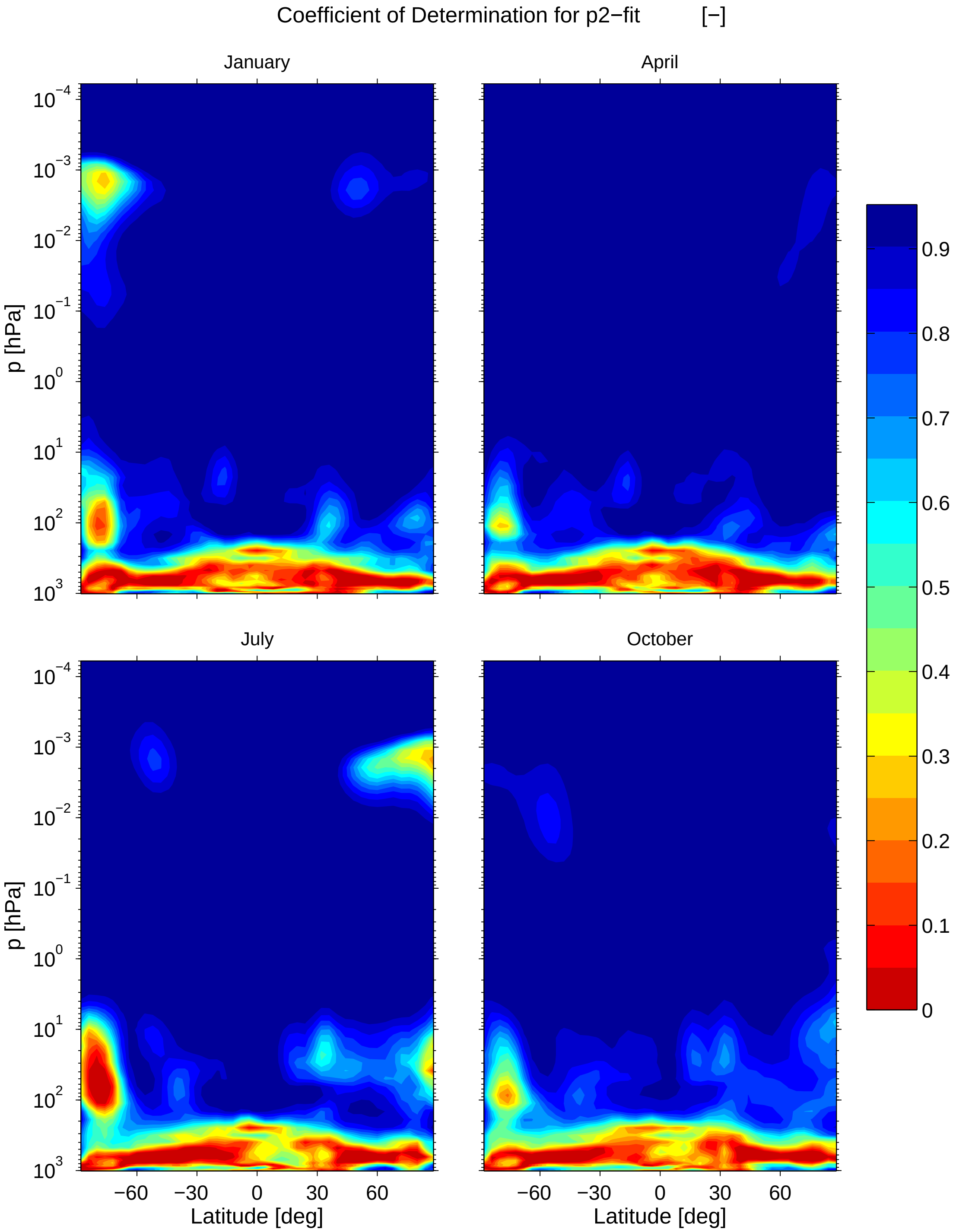

Figure 4.3: Vertical cross-section of the coefficient of determination R^2 obtained from polynomial curve fitting. R^2 indicates how much variation of Q_{rad} can be explained by the model function $P_2 = a_0 + a_1\,T' + a_2\,T'^2$.

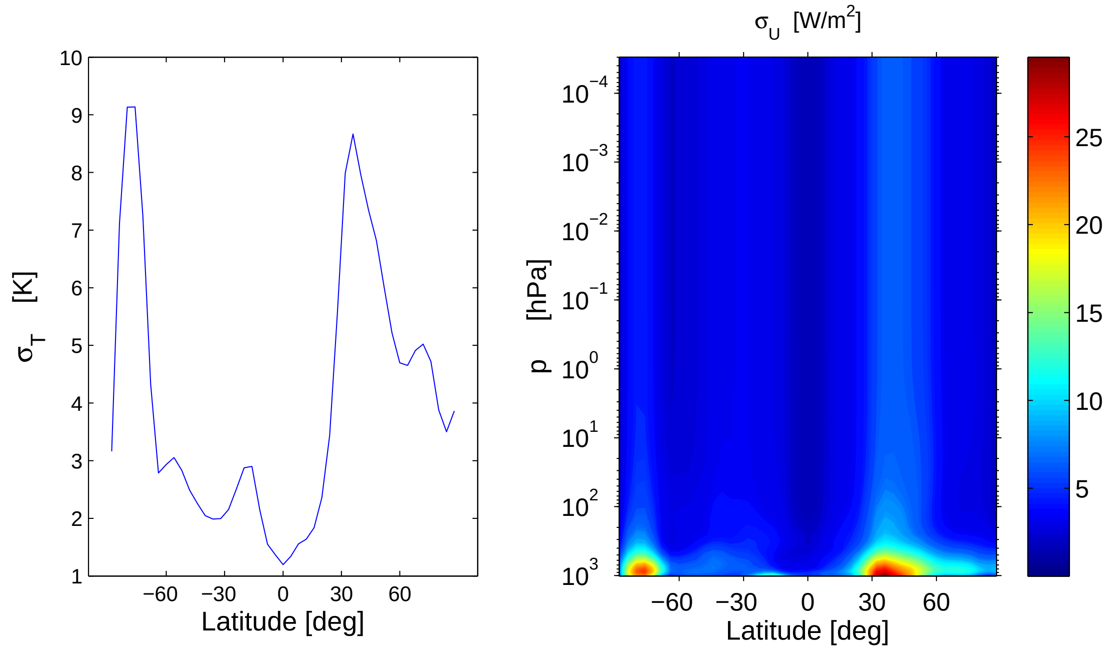

Figure 4.4: Left: σ_T in the first model layer above ground (≈ 100 m height) in January. Large values of σ_T are found around $\phi = -75°$ and $\phi = +40°$. **Right:** Variations of U_{tot} as a function of latitude and altitude for the same period. Comparing both panels, the latitudinal distribution of σ_U and σ_T corresponds well.

and D_{tot} in the MLT are indeed generated non-locally in the troposphere. The left-hand side panel shows $\sigma_T(\phi)$ at about 100 m above ground for January while the right-hand side panel shows the corresponding standard deviation of U_{tot} for the whole vertical domain. It is plausible that large values of σ_T around $\phi = -75°$and $\phi = 40°$ arise from weather systems (baroclinic Rossby waves). Affecting U_{tot} and D_{tot}, these tropospheric temperature variations influence the cooling rate in the mesopause region. The effect is small with maximum variations of Q_{rad} of about ± 0.15 K/day (5% of Q_{rad}). It refers to the case of RW-induced cooling rate variations that has been discussed in the context of Fig. 2.7.

Hereafter, all conclusions refer to regions with $R^2 \geq 0.9$. Thus the troposphere, the lower stratosphere and the polar summer mesopause region are not further considered.

4.6 Global and seasonal distribution of additional cooling rates

We define the variations of the radiative cooling rate due to atmospheric waves by the standard deviation

$$\sigma_Q = \sqrt{\langle [(Q'_{\mathrm{rad}} + Q''_{\mathrm{rad}})^{\,2}] \rangle}\,. \tag{4.12}$$

The dependency of σ_Q on latitude and altitude for different seasons is shown in Fig. 4.5, where $Q'_{\mathrm{rad}} \approx a_1\, T'$ and $Q''_{\mathrm{rad}} \approx a_2\, T'^{\,2}$ are reconstructed from the fitting procedure.

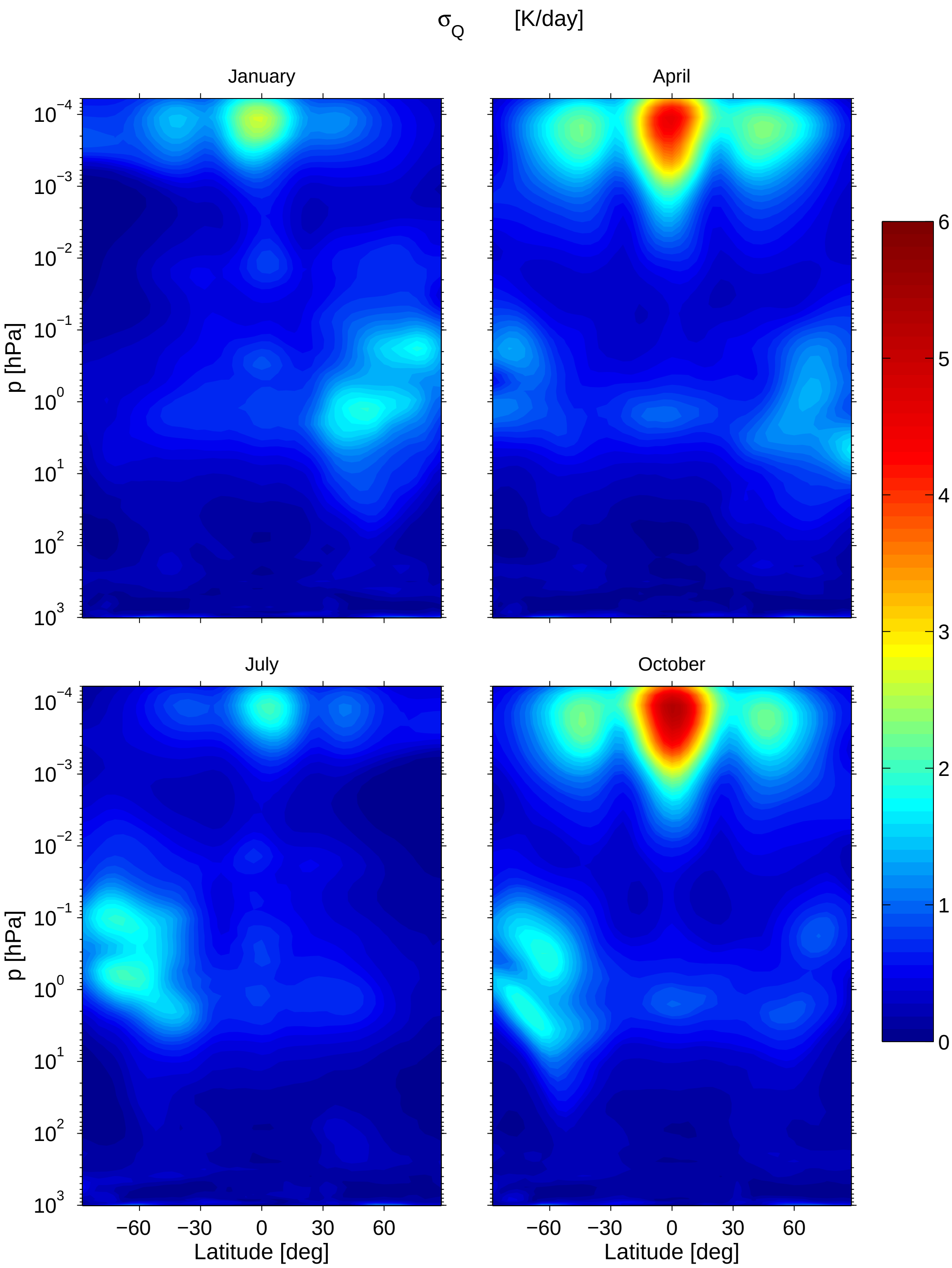

Figure 4.5: Vertical cross-section of the variations of the radiative cooling rate σ_Q due to waves with periods shorter than 10 days. Largest values of σ_Q show up in the equatorial MLT during equinox. Further important contributions are located at the poles around the stratopause and the lower mesosphere.

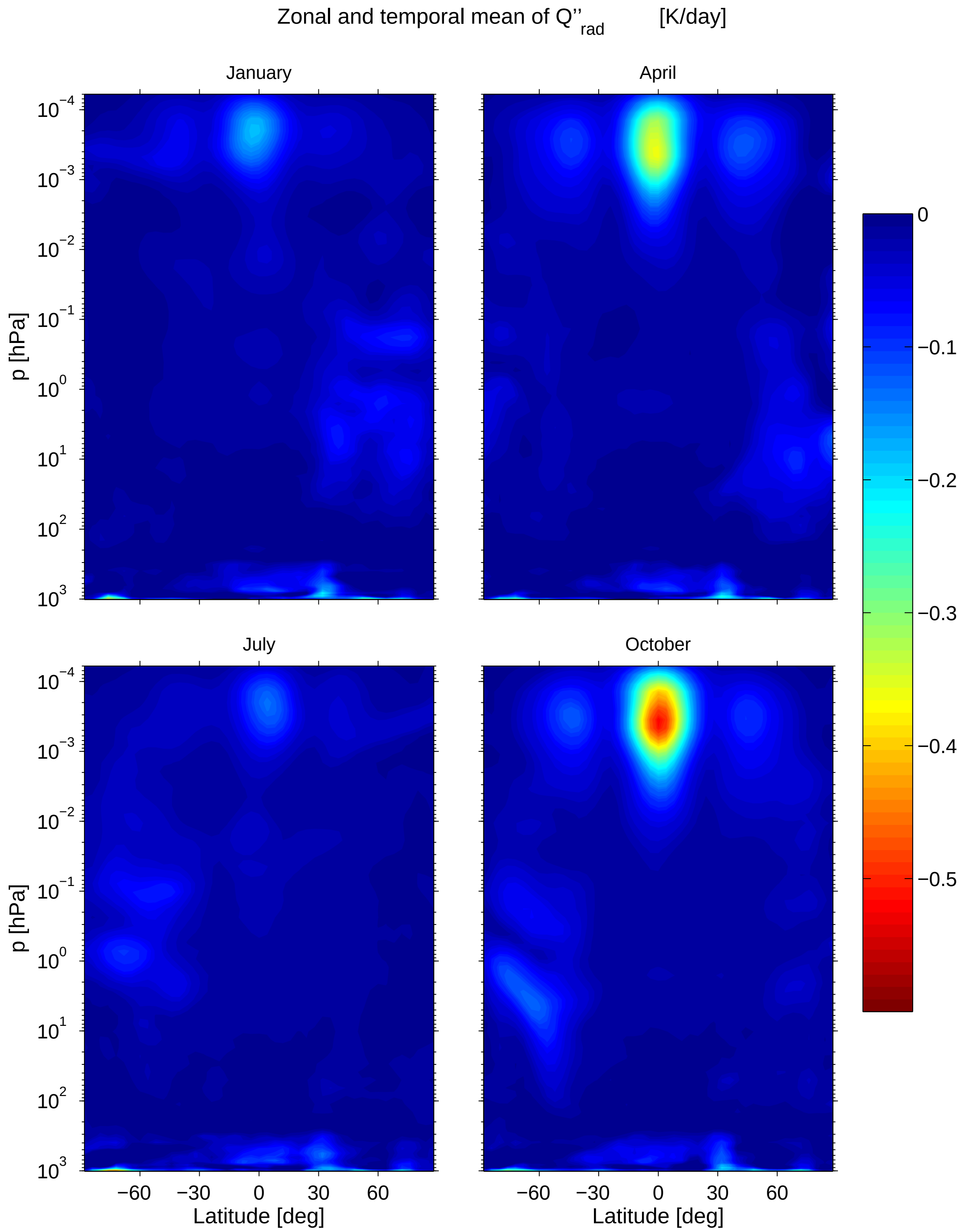

Figure 4.6: Vertical cross-section of $\langle[Q''_{\text{rad}}]\rangle$. It is negative by definition. Significant values are only found in regions associated with strong TW activity during equinox.

The largest cooling rate variations σ_Q can be found in the region we associate with strongest tidal wave activity. Around the equator, maximum values of $\sigma_Q = 5.4$ K/day are found. In periods of strong wave activity the modulation of the cooling rate can exceed the background cooling rate. Variations of the cooling rate caused by RWs amount to 2 K/day around the polar stratopause. Furthermore, values of $\sigma_Q = 0.5$ K/day are widely common in the mesosphere for all latitudes. The similar distribution of large σ_T and σ_Q implies that the prefactors a_1 and a_2 are only weakly varying with latitude and height.

The additional net cooling is presented in Fig. 4.6. Values of $\langle[Q''_{\mathrm{rad}}]\rangle$ are roughly one order of magnitude smaller than σ_Q. In April the maximum additional net cooling is 0.36 K/day and in October 0.52 K/day due to tidal waves in the equatorial lower thermosphere. Seasonal differences arise from larger tidal temperature amplitudes in October than in April. RWs generate additional net cooling mainly in the polar lower mesosphere with values up to 0.1 K/day.

4.7 Cooling rate coefficients in KMCM

Figure 4.7 shows the global distribution of the cooling rate coefficient a_1 from Eq. (4.10) for different seasons. A comparison with Fig. 4.1 reveals the strong dependency of a_1 on T_{r}. Cooling rate coefficients calculated with Curtis matrices by Zhu [1993] (without scale dependence, i.e. for infinite vertical wavelength) show the same vertical structure but with significant larger values, e.g. twice our values around the stratopause and five times larger values in the lower thermosphere. However, our results are in good agreement with Dickinson [1973] for the height range between $30 - 70$ km.

As a next step, a parameterization for the horizontally averaged a_1 is derived. This parameterization is called α_1 and depends in principle on all four absorber bands

$$\alpha_1 = \sum_k \alpha_1^k \,. \tag{4.13}$$

Different functional relationships of α_1^k are tested. The temperature dependency is incorporated as T_{r}^3 or as the first Taylor expansion coefficient of the frequency averaged Planck function B_1^k (see Eq. (4.7)). Also we consider non-LTE as $(1 - \overline{\omega}_{\mathrm{s}}^k)$ and the mass mixing ratio as ρ_{a}^k/ρ. The band strength $\overline{K}_{\mathrm{r}}^k$ is used as a tuning parameter.

For the MLT, a good parameterization is achieved for CO_2 alone

$$\alpha_1 = \alpha_1^4 = \overline{K}^4 \frac{\rho_{\mathrm{a}}^4}{\rho} \,(1 - \overline{\omega}_{\mathrm{s}}^4)\, B_1^4 \,. \tag{4.14}$$

A comparison of the horizontally averaged a_1 with different parameterizations α_1 is given in Fig. 4.8. It illustrates that T_{r}^3 is inadequate to describe a_1 in the lower thermosphere due to the different non-linearity of $\int B_\nu \, d\nu$ for small frequency bands and high temper-

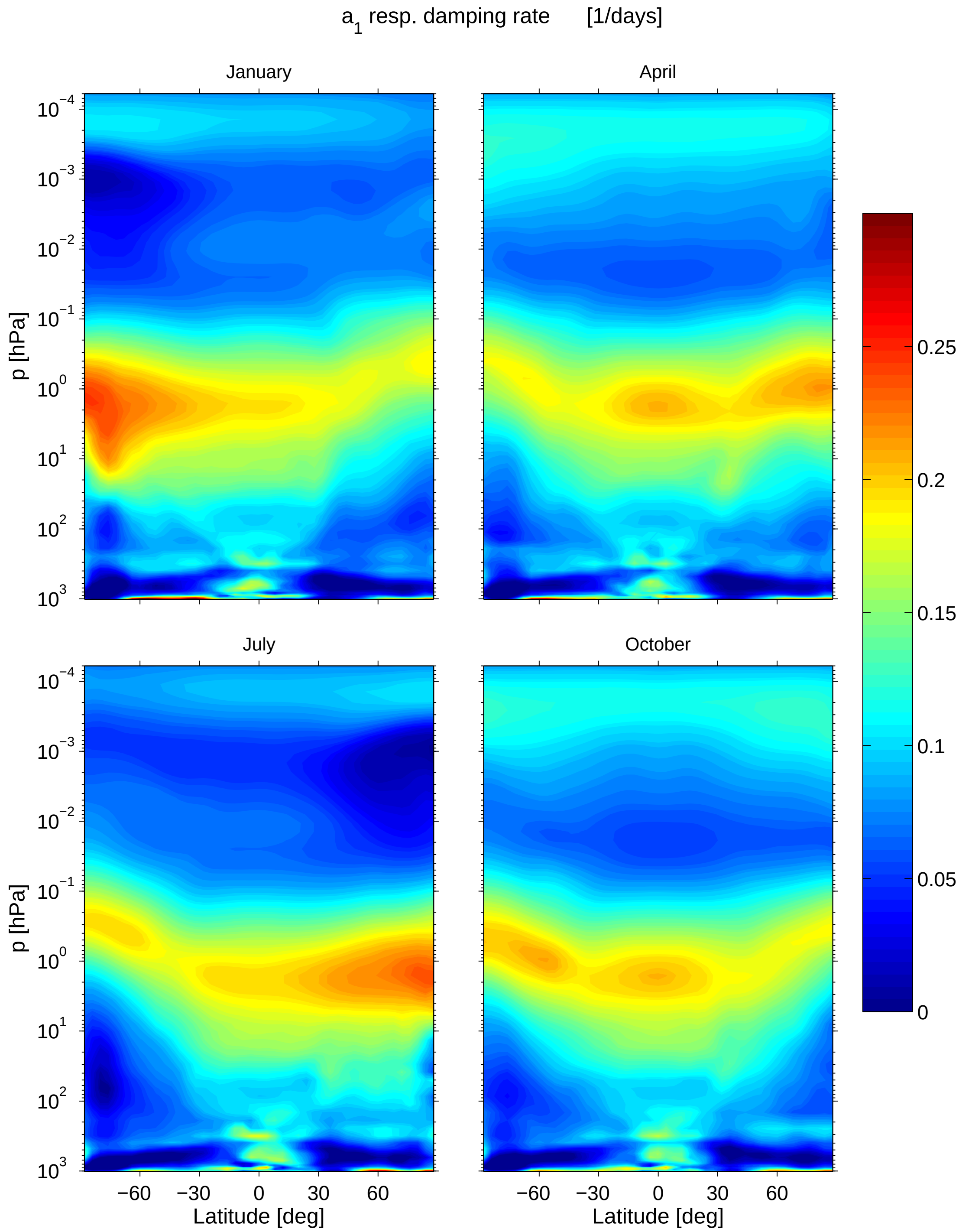

Figure 4.7: Vertical cross-section of the first cooling rate coefficient a_1. A comparison with Fig. 4.1 demonstrates that most of latitudinal and vertical variations are linked to the background temperature T_r. Typical relaxation times are 5 days in the stratopause, 10 days in the stratosphere, mesosphere and lower thermosphere as well as a maximum of 17 days in the mesopause.

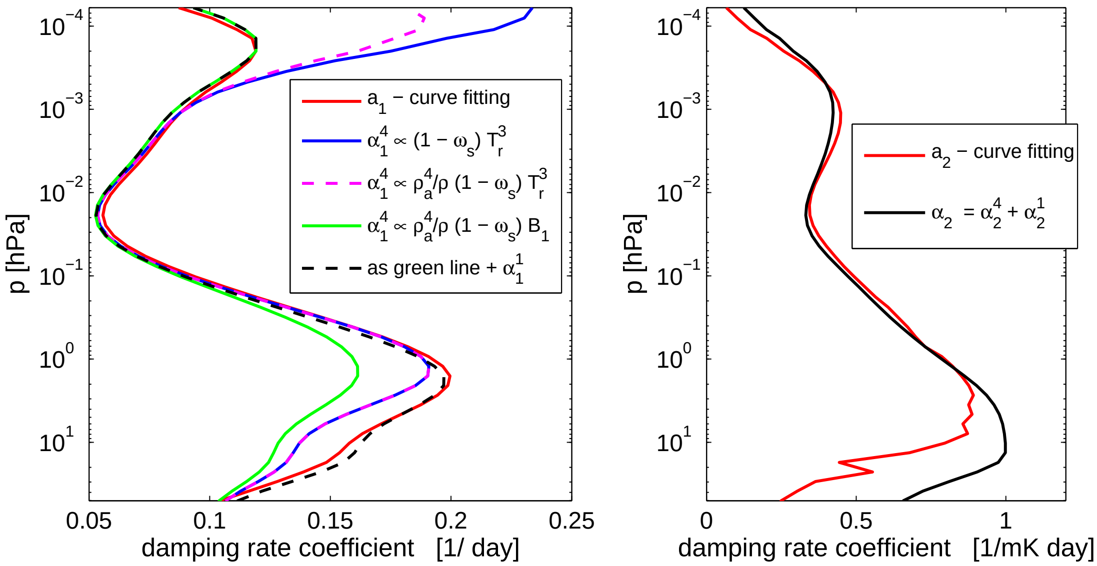

Figure 4.8: Left: Different parameterizations for the meridional averaged a_1 for October (compare to Fig. 4.7). All attempts to describe the lower thermosphere with T_r^3 fail. Including non-LTE and mixing ratios for CO_2 and O_3, the best result is found with a Taylor expansion of the Planck function (black line). **Right:** Meridional averaged a_2 and its the best parameterization α_2 for October. The error in the stratosphere (below 1 hPa) arises from a bad estimation of a_2.

atures (≈ 400 K). To achieve a good approximation in the stratosphere too, the cooling rate coefficient of ozone (analogous to Eq. (4.14)) is added

$$\alpha_1 = \alpha_1^4 + \alpha_1^1 \,. \tag{4.15}$$

The evaluation of Eq. (4.15) is given by the dashed black line in Fig. 4.8. The relative error is smaller than 10%.

The same procedure is done for α_2 using the second Taylor expansion coefficient B_2^k

$$\alpha_2^k = \overline{K}_\mathrm{r}^k \frac{\rho_\mathrm{a}^k}{\rho} (1 - \overline{\omega}_{\mathrm{s,r}}^k) B_2^k \,, \tag{4.16}$$

$$\alpha_2 = \alpha_2^4 + \alpha_2^1 \,. \tag{4.17}$$

Above the equatorial stratopause the relative error of this parameterization is less than 10 % up to the Mesopause, see Fig. 4.8.

Having α_2 at hand it is possible to calculate $\langle [Q''_\mathrm{rad}] \rangle$ for any given σ_T

$$\langle [Q''_\mathrm{rad}] \rangle = \alpha_2 \, \sigma_T^2 \,. \tag{4.18}$$

This was done for small-scale temperature fluctuations associated with GWs taken from Kutepov et al. [2007]. These authors applied a model “which randomly generates individual temperature profiles reminiscent of instantaneous measurements during periods

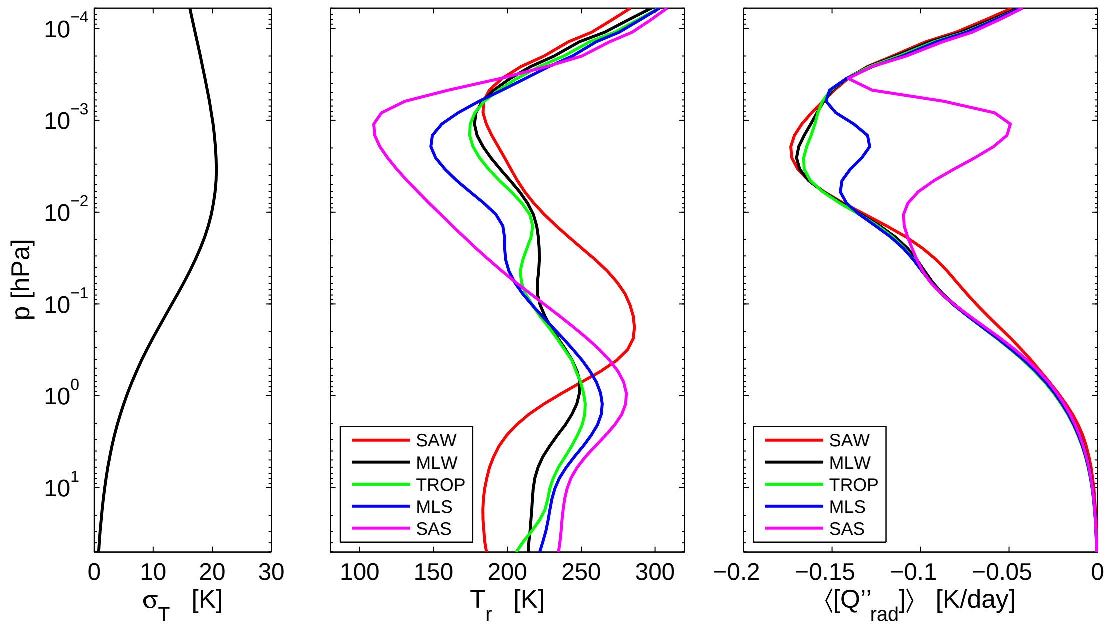

Figure 4.9: Left: Rebuild of the σ_T profile caused by a broad spectrum of GWs analogously to Kutepov et al. [2007]. **Middle:** T_r for NH summer for five different latitudes as simulated by KMCM (see Fig. 4.1 in July, same color coding as used in Kutepov et al. [2007]). **Right:** Estimates of the additional net cooling rate from Eq. (4.18) that would occur for σ_T due to GWs and different background states from KMCM.

of strong GW activity, whose statistical properties agree with observed spectra." The σ_T of Kutepov et al. [2007] has been rebuild with focus on the maximum value of ≈ 21 K at an altitude of 90 km. α_2 was computed from the zonally and temporally averaged KMCM data set (July) for five different latitudes: $-72°$ for subantarctic winter (SAW), $-40°$ for midlatitude winter (MLW), $0°$ for the tropics (TROP), $40°$ for midlatitude summer (MLS) and $72°$ for subartic summer (SAS).

A comparison of the input parameter T_r that is given in the middle panel of Fig. 4.9 with Kutepov et al. [2007] shows a good quantitative agreement. The vertical structure of the additional net cooling rates are found to be consistent but absolute values are roughly one order of magnitude smaller. The absolute amplitude of the additional net cooling is 0.2 K/day in the winter hemisphere and the tropics according to the present estimation.

A possible explanation for our smaller additional net cooling is the smaller overall cooling rate computed with KMCM. For example at 90 km and the SAW profile, KMCM yields $T_\mathrm{r} = 193$ K and $Q_\mathrm{rad} = -1$ K/day whereas Kutepov et al. [2007] find $T_\mathrm{r} = 197$ K and $Q_\mathrm{rad} = -7.5$ K/day. For the MLW profile, KMCM computes $T_\mathrm{r} = 184$ K and $Q_\mathrm{rad} = 0.5$ K/day and Kutepov et al. [2007] obtain $T_\mathrm{r} = 190$ K and $Q_\mathrm{rad} = -3.5$ K/day. For more details, see $Q_\mathrm{rad,r}$ from KMCM in Fig.A.3 in the appendix. We believe that the use of the band strengths $\overline{K}^k$ as a tuning parameter in KMCM with focus on a reasonable atmospheric dynamic may yield the underestimation of the cooling rate in the MLT. To be fair, one also has to note that the radiative transfer code of Kutepov et al. [2007]

has not yet been interactively run in a middle atmosphere GCM. Finally, Kutepov et al. [2007] state that the product of collision quenching rate and atomic oxygen concentration has an important role in the amount of radiative cooling by CO_2. Assuming the lowest (instead of the highest, difference of factor 4) accepted quenching rate, Kutepov et al. [2007] found maximum additional cooling reduced from 2.5 → 1 K/day.

A recent study of Kutepov et al. [2013] considers, moreover, a modulation of the volume mixing ratios (VMRs) $[O(^3p)]$ and $[CO_2]$ by GWs

$$[M]' = \frac{\partial_z [M]}{N^2} T' \,. \tag{4.19}$$

The effect has been observed for tides at the equator by satellites [Smith et al., 2010]. Kutepov et al. [2013] found an increase of the additional net cooling mainly contributed by variations of T' and $[O(^3p)]'$ whereas $[CO_2]'$ has the opposite effect. A maximum additional net cooling of 4 K/day is obtained in periods of strong GW activity.

4.8 Radiative damping of resolved tidal waves

4.8.1 Tidal waves without radiative damping

In order to study tidal waves that are not damped by long-wave radiation in the MLT, we use a modified model setup of KMCM. More specifically, we compute the long-wave radiative transfer not for the complete temperature field but only for the zonal-mean temperature. To maintain the dynamics at lower altitudes where the TWs are mainly generated, we choose

$$Q_{\mathrm{rad}} = \begin{cases} Q_{\mathrm{rad}}(T) & p > 0.1 \text{ hPa} \\ Q_{\mathrm{rad}}([T]) & p \leq 0.1 \text{ hPa} \end{cases} \tag{4.20}$$

with the transition level of 0.1 hPa. Our tides are still damped by other processes (vertical and horizontal diffusion, interaction with parameterized GWs). Nevertheless, the terms "damped" and "undamped" shall refer hereinafter only to the radiative damping process.

4.8.2 Extracting the migrating (semi-) diurnal tide with Fourier analyses

In Sec. 3.5 it was pointed out that radiative damping depends on the tidal equivalent depths, which are larger for the gravest semidiurnal modes as for the diurnal modes. To extract this difference, a Fourier analysis in longitude and another one in time is performed on damped and undamped tides. The migrating diurnal tidal temperature variation is given by

$$T'^{\,1,1} = \widehat{T}_{\mathrm{R}} \cos(\omega_{\mathrm{E}}\, t + \lambda) + \widehat{T}_{\mathrm{I}} \sin(\omega_{\mathrm{E}}\, t + \lambda) \,, \tag{4.21}$$

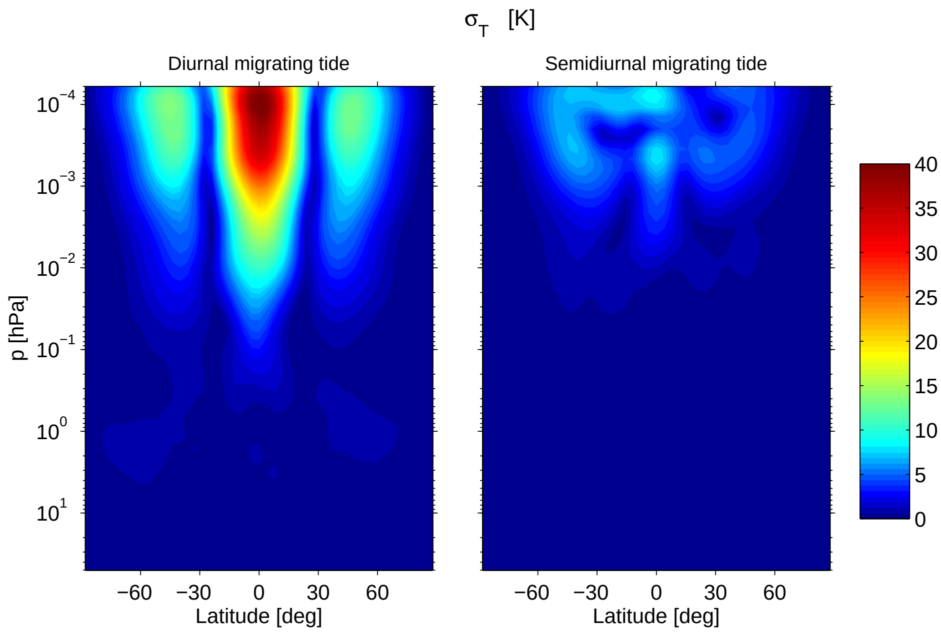

Figure 4.10: Vertical cross-section of the temperature standard deviation in October that is spectrally filtered (left) for zonal wavenumber one and wave period of one day and (right) zonal wavenumber two and wave period of a half day. The temperature variations with periods of one day are associated with the migrating diurnal tide and show a distinct modal structure due to the involved Hough functions. The migrating semidiurnal tide show a pronounced structure which not only varies with latitude but also in the vertical.

where $\widehat{T}_{\mathrm{R}}$ and $\widehat{T}_{\mathrm{I}}$ are the Fourier coefficients depending latitude and height. The migrating semidiurnal temperature variation $T'^{\,2,2}$ is equivalently represented by $\omega = 2\,\omega_{\mathrm{E}}$ and $s = 2$. The standard deviation of the diurnal migrating tidal temperature amplitude is

$$\sigma_{T^{\,1,1}} = \sqrt{\langle [(T'^{\,1,1})^2] \rangle}\,. \tag{4.22}$$

The Fourier analyses for damped tides are based on the original data set of the period of the first 10 days in October. The analyses are carried out for each October of the five model years and are subsequently averaged. Using the modified model setup for undamped tides, KMCM simulations are performed beginning with the initial state vector of October 1st of the original data set and ending on October 10th for each realization.

Before considering the radiative damping process of σ_T, classical linear tidal theory is linked to the findings of damped diurnal and semidiurnal σ_T from KMCM simulations.

4.8.3 The migrating (semi-) diurnal tide in KMCM

Figure 4.10 shows $\sigma_{T^{\,1,1}}$ and $\sigma_{T^{\,2,2}}$ for October. The left-hand side panel due to the diurnal migrating tide can be compared to Figs. 3.2 and 3.3 which are calculated for equinox conditions. Both estimates show a similar latitudinal structure of maximum

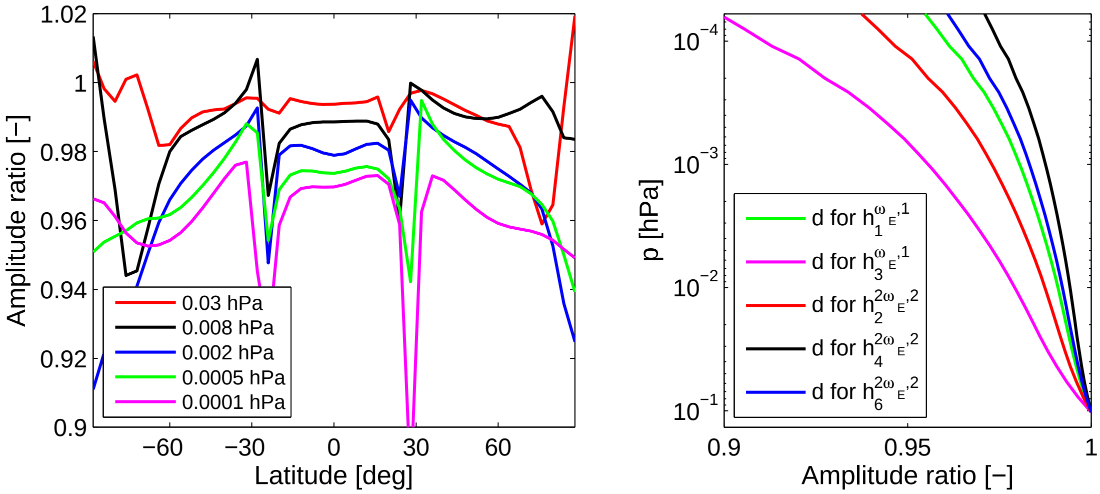

Figure 4.11: Left: Ratios of damped to undamped temperature amplitude of the resolved migrating diurnal tide as a function of latitude for five different pressure levels in October from KMCM. **Right:** Improved semi-analytical (see text) ratios of damped to undamped temperature amplitude for different Hough modes of the migrating diurnal and semidiurnal tide as function of altitude for October.

temperature amplitudes at the equator with smaller maxima around ±45° in KMCM and ±35° in LC. These structures are found to be uniform over a wide altitude range above the stratosphere. Amplitude values increase exponentially with height and are in good agreement for KMCM and LC. The relevant involved diurnal Hough modes could be identified by a decomposition $\sigma_{T^{1,1}}$ into Hough functions analogue to a Fourier analysis. Here, we just compare the curve shapes of single Hough functions (see LC) from tidal theory with $\sigma_{T^{1,1}}$ taken from KMCM. In agreement with theory the functions $\Theta_1^{\omega_\mathrm{E},1}$, $\Theta_3^{\omega_\mathrm{E},1}$ and $\Theta_5^{\omega_\mathrm{E},1}$ match pretty well the three aforementioned maxima. Hough functions of the diurnal migrating tide with negative index have to be unimportant because no maxima are found at high latitudes. The same conclusion is made for antisymmetric Hough functions that could not account for the maximum around the equator.

On average, $\sigma_{T^{2,2}}$ is roughly four times smaller than $\sigma_{T^{1,1}}$. This is caused by the exponential decay in the mesosphere of the Hough mode $\Theta_2^{2\omega_\mathrm{E},2}$. It was noted that $\Theta_4^{2\omega_\mathrm{E},2}$ is dominant in the lower thermosphere. Indeed, the structure of $\sigma_{T^{2,2}}$ can arise from this Hough mode around $p = 0.0005$ and $p = 0.0001$ hPa. The vertical irregularity of $\sigma_{T^{2,2}}$ can be explained by the high sensitivity of $\Theta_4^{2\omega_\mathrm{E},2}$ due to modest changes of background winds and temperature as mentioned by Hong and Lindzen [1976].

4.8.4 Radiative damping of the migrating (semi-) diurnal tide in KMCM

Figure 4.11 shows the amplitude ratio of damped over undamped $\sigma_{T^{1,1}}$ for different pressure levels. A value greater than one means a reduced wave amplitude although radiative damping of the wave is switched off.

For each pressure level the amplitude ratios are constant around the equator and slowly decreasing between ±30° to ±60°. For other latitudes a more complicated behavior is obtained containing also values above one implying another process causing the amplitude change. Around the equator the amplitude ratio is about 97 % for a vertical propagation path of $0.1 \leq p \leq 0.0001$ hPa. The predicted ratio of 90 % from pure analytical calculations (Eq. (3.27) and Fig. 3.4) for the same vertical propagation distance is significantly smaller. This error is caused by an overestimation of the analytical cooling rate coefficient α due to the T_r^3 dependency. A better description is achieved using the parameterization α_1 (from Eq. (4.15); see Fig. 4.8 left, dashed black line). The amplitude ratio d is found by integrating $\alpha_1(z)$ numerically

$$d = \exp\left\{ -\frac{m_\mathrm{r}^2 + \frac{1}{4H^2}}{m_\mathrm{r}} \frac{H}{2\,\omega} \int_{z_\mathrm{s}}^{z} \alpha_1 \, dz' \right\} , \tag{4.23}$$

where m_r is the vertical wavelength of a particular Hough mode (see Eq. 3.24). The improved amplitude ratios d are shown on the right-hand side of Fig. 4.8. The ratio for the Hough mode $\Theta_1^{1\omega_\mathrm{E},1}$ is about 96 % at 0.0001 hPa. This result is in good agreement with the ratio that is obtained for the resolved migrating diurnal tide from KMCM simulations implying that $\Theta_1^{1\omega_\mathrm{E},1}$ is, in agreement with linear theory, the dominant migrating diurnal mode in KMCM. For the migrating semidiurnal tide the variations of amplitude ratios are larger and more irregularly (not shown). It is not possible to distinguish amplitude damping from feedbacks on wave propagation due to an altered background.

The technical measure that is explained in Sec. 4.8.1 acts in two ways on the waves. Since no energy of the wave is lost to the radiation field, which would be transported into space or other air layers, σ_T increases with time until a new equilibrium state is reached. This is observed in KMCM simulations. Considering dissipative processes like molecular diffusion of heat and momentum or turbulence due to wave breaking, the additional energy of the tides is deposited locally and, therefore, heats the MLT. In our scenario (10 days in early October) an averaged temperature increase is observed, reaching 2.5 K in the lower thermosphere, comparing the modified background state to the original one. Strong variations of the amplitude ratios of a tide, which are a sum of ratios over all involved Hough modes, are therefore generated not only by a change in amplitude but also by alterations in wavelength and phase of particular Hough modes. In the case of the migrating diurnal tide, a high sensitivity of wave parameter mainly occur for less important Hough modes and, thus, strong variations of the amplitude ratios appear only in the absence of $\Theta_1^{\omega_\mathrm{E},1}$, $\Theta_3^{\omega_\mathrm{E},1}$ and $\Theta_5^{\omega_\mathrm{E},1}$ at high latitudes (see left-hand side panel of Fig. 4.11).

Hence, in case of resolved waves (e.g. the migrating semidiurnal tide in the MLT), whose propagation is sensitive to background fields, no quantitative statement can be given about the amount of damping of the amplitude by radiation. It may be asked, whether a comparison of amplitudes of highly sensitive waves is meaningful at all when switching off radiative damping modifies the background state and, therefore, the conditions for wave propagation.

4.9 Summary

For the interaction of TWs and RWs with thermal radiation in KMCM it has been shown that:

- Radiative cooling rates in the MLT from KMCM simulations can be described approximately by $Q_{\mathrm{rad}} = a_0 + a_1 T' + a_2 T'^2$
- The maximum value of the variation of the radiative cooling rate is 5.4 K/day for TWs and 2 K/day for RWs in October.
- The maximum value for the additional net radiative cooling is 0.5 K/day for TWs and 0.1 K/day for RWs in October.
- 0.2 K/day additional net radiative cooling is expected from GW activity in KMCM simulations.
- The temperature amplitude of the resolved migrating diurnal tide is radiatively damped by 4% between 65 – 110 km height.

5 Conclusion

5.1 Summary

The interaction of long-wave radiative transfer with internal gravity waves and thermal tides in the middle atmosphere was investigated.

The fundamental principle how a temperature perturbation associated with a gravity wave, a tidal wave or a Rossby wave act on long-wave radiative transfer is analyzed with the radiative transfer equations in two-stream approximation. An additional radiative net cooling can occur for gravity and tidal waves in the mesosphere and the lower thermosphere. The effect of non-LTE limits the additional net cooling. The amount of additional net cooling does not depend on any wave property other than the amplitude. It was shown that only tropospheric and stratospheric waves, like Rossby waves, are able to significantly affect the absolute upward long-wave radiation flux at higher altitudes. The concept of scale-dependent radiative cooling rates proposed by Fels [1982] was analyzed and found to be questionable in the middle atmosphere.

Height-dependent radiative damping in WKB approximation was introduced to the linear theory of mid-frequency gravity waves and tidal waves. The solution of the height-depending radiative damping is similar to that derived for wave damping by diffusion. The amount of radiative damping increases for stronger thermal emission and a longer residence time of the wave in the atmosphere. The latter depends on source and breaking height of the wave and its vertical group velocity.

The amount of additional net cooling was quantified for a realistic background state and resolved thermal tides and Rossby waves with KMCM simulations. The maximum values for the additional net radiative cooling are 0.5 K/day for tides in the lower thermosphere during equinox and 0.1 K/day for Rossby waves in the lower winter mesosphere. The additional net cooling for gravity waves was estimated from a model-based cooling rate parameterization combined with a reasonable temperature variation profile. A maximum value of 0.2 K/day was obtained for phases of strong gravity wave activity in the winter and equatorial mesosphere. There is a strong discrepancy between our estimate for the additional net cooling due to gravity waves and the result by Kutepov et al. [2007].

Using simulations with KMCM, the amount of radiative damping of the migrating diurnal tide was estimated. For this purpose, this tide was filtered from the total resolved wave spectrum by Fourier analyses and a technical method was presented that allow to study resolved radiatively undamped tides in a limited altitude range. The radiative damping of the migrating diurnal tide was found to be 4% for a propagation path from 65 km to 110 km height.

5.2 Outlook

The first point concerns improvements to increase the accuracy of the estimations of additional radiative net cooling and radiative wave damping based on numerical computations with the KMCM. A comparison between the long-wave radiative cooling rates from KMCM and Fomichev et al. [2007] yields that they are quantitatively consistent from the troposphere up to the mesosphere whereas above the vertical structure of the cooling rate is upwardly shifted in KMCM. The latter accounts at least partially for the under-estimating of long-wave radiative cooling of both background and waves in the mesopause and the lower thermosphere. Hence, we suggest to perform a validation of the radiative transfer scheme in KMCM against the code of Fomichev et al. [2007] in order to better constrain the adjustable parameters of the KMCM radiation scheme. Furthermore, the effect of mixing ratio variations of atomic oxygen and carbon dioxide due to resolved waves should be taken into account as was done in Kutepov et al. [2013] for gravity waves since such variations may cause a significant increase of additional radiative net cooling. For gravity waves, the additional radiative net cooling and radiative amplitude damping should also be quantified using a high spatial resolution version of KMCM with resolved gravity waves.

The second point is about the technique to estimate the amount of radiative damping using KMCM simulations. It should be amended in a way to ensure that waves, whether damped or not, propagate in the same background state. Therefore, wave-dependent processes like molecular diffusion of heat and momentum that affect the background state should be reasonably prescribed for both the original and the modified setup. When the aforementioned measure is implemented, the calculation of radiative damping for a particular Hough mode might be conceivable by a decomposition of the diurnal or semidiurnal tidal temperature perturbation in Hough functions.

The last point refers to related fields of interests. Recently a model version of KMCM was established that generates the *Quasi-biennial Oscillation* with resolved equatorial waves. This oscillation is driven by horizontal momentum that is vertically transported by the waves and transferred to the mean flow by dissipative processes. Therefore, an investigation of the role of radiative damping, which is one of these dissipative processes, in the Quasi-biennial Oscillation would be a reasonable extension of this work.

Bibliography

Richard Asselin. Frequency Filter for Time Integrations. *Monthly Weather Review*, 100, 1972. 4.2

E. Becker and U. Burkhardt. Nonlinear Horizontal Diffusion for GCMs. *Monthly Weather Review*, 135:1439–1454, 2007. doi: 10.1175/MWR3348.1. 4.2

Erich Becker. Frictional Heating in Global Climate Models. *Monthly Weather Review*, 131, 2003. 4.2

Erich Becker and Charles McLandress. Consistent Scale Interaction of Gravity Waves in the Doppler Spread Parameterization. *Journal of the Atmospheric Sciences*, 66: 1434–1449, 2009. doi: 10.1175/2008JAS2810.1. 4.2

Robert E. Dickinson. Method of parameterization for infrared cooling between altitudes of 30 and 70 kilometers. *Journal of Geophysical Research*, 78(21): 4451–4457, 1973. ISSN 2156-2202. doi: 10.1029/JC078i021p04451. URL http://dx.doi.org/10.1029/JC078i021p04451. 4.7

S. B. Fels. A parameterization of scale-dependent radiative damping rates in the middle atmosphere. *Journal of Atmospheric Sciences*, 39:1141–1152, May 1982. doi: 10.1175/1520-0469(1982)039<1141:APOSDR>2.0.CO;2. 1.1, 2.7, 5.1

S. B. Fels. The Radiative Damping of Short Vertical Scale Waves in the Mesosphere. *Journal of Atmospheric Sciences*, 41:1755–1764, May 1984. doi: 10.1175/1520-0469(1984)041<1755:TRDOSV>2.0.CO;2. 1.1

V. I. Fomichev, A. I. Jonsson, J. de Grandpre, S. R. Beagley, C. McLandress, K. Semeniuk, and T. G. Shepherd. Response of the Middle Atmosphere to CO2 Doubling: Results from the Canadian Middle Atmosphere Model. *Journal of Climate*, 20:1121–1144, 2007. doi: 10.1175/JCLI4030.1. URL http://dx.doi.org/10.1175/JCLI4030.1. 5.2

Jeffrey M. Forbes. Middle atmosphere tides. *Journal of Atmospheric and Terrestrial Physics*, 46(11):1049 – 1067, 1984. ISSN 0021-9169. doi: http://dx.doi.org/10.1016/0021-9169(84)90008-4. URL http://www.sciencedirect.com/science/article/pii/0021916984900084. 3.5, 3.5

David C. Fritts and M. Joan Alexander. Gravity wave dynamics and effects in the middle atmosphere. *Reviews of Geophysics*, 41(1):n/a–n/a, 2003. ISSN 1944-9208. doi: 10.1029/2001RG000106. URL http://dx.doi.org/10.1029/2001RG000106. 1.1, 3.2

M. E. Hagan, J. L. Chang, and S. K. Avery. Global-scale wave model estimates of nonmigrating tidal effects. *Journal of Geophysical Research: Atmospheres*, 102(D14):16439–16452, 1997. ISSN 2156-2202. doi: 10.1029/97JD01269. URL http://dx.doi.org/10.1029/97JD01269. 3.5

Siu-Shung Hong and Richard S. Lindzen. Solar Semidiurnal Tide in the Thermosphere. *Journal of the Atmospheric Sciences*, 33:135–153, 1976. doi: 10.1175/1520-0469(1976)033. 3.5, 4.8.3

B. J. Hoskins and A. J. Simmons. A multi-layer spectral model and the semi-implicit method. *Quarterly Journal of the Royal Meteorological Society*, 101(429):637–655, 1975. ISSN 1477-870X. doi: 10.1002/qj.49710142918. URL http://dx.doi.org/10.1002/qj.49710142918. 4.2

Rahel Knöpfel and Erich Becker. An idealized radiative transfer scheme for use in a mechanistic general circulation model from the surface up to the mesopause region. *Journal of Quantitative Spectroscopy and Radiative Transfer*, 112(9):1460 – 1478, 2011. ISSN 0022-4073. doi: http://dx.doi.org/10.1016/j.jqsrt.2011.02.014. URL http://www.sciencedirect.com/science/article/pii/S0022407311000926. 2.7, 4.2, A.1

Alexander A. Kutepov, Artem G. Feofilov, Alexander S. Medvedev, Adalbert W. A. Pauldrach, and Paul Hartogh. Small-scale temperature fluctuations associated with gravity waves cause additional radiative cooling of mesopause the region. *Geophysical Research Letters*, 34(24):n/a–n/a, 2007. ISSN 1944-8007. doi: 10.1029/2007GL032392. URL http://dx.doi.org/10.1029/2007GL032392. (document), 1.1, 2.7, 2.9, 4.7, 4.9, 5.1

AlexanderA. Kutepov, ArtemG. Feofilov, AlexanderS. Medvedev, Uwe Berger, Martin Kaufmann, and AdalbertW.A. Pauldrach. Infra-red Radiative Cooling/Heating of the Mesosphere and Lower Thermosphere Due to the Small-Scale Temperature Fluctuations Associated with Gravity Waves. In Franz-Josef Lübken, editor, *Climate and Weather of the Sun-Earth System (CAWSES)*, Springer Atmospheric Sciences, pages 429–442. Springer Netherlands, 2013. ISBN 978-94-007-4347-2. doi: 10.1007/978-94-007-4348-923. URL http://dx.doi.org/10.1007/978-94-007-4348-923. 1.1, 2.9, 4.7, 4.7, 5.2

R. S. Lindzen. Thermally driven diurnal tide in the atmosphere. *Quarterly Journal of the Royal Meteorological Society*, 93(395):18–42, 1967. ISSN 1477-870X. doi: 10.1002/qj.49709339503. URL http://dx.doi.org/10.1002/qj.49709339503. 3.2, 3.3

R S Lindzen. Atmospheric Tides. *Annual Review of Earth and Planetary Sciences*, 7(1):199–225, 1979. doi: 10.1146/annurev.ea.07.050179.001215. URL http://www.annualreviews.org/doi/abs/10.1146/annurev.ea.07.050179.001215. 3.4, 3.5

RichardS. Lindzen and Sydney Chapman. Atmospheric tides. *Space Science Reviews*, 10(1):3–188, 1969. ISSN 0038-6308. doi: 10.1007/BF00171584. URL http://dx.doi.org/10.1007/BF00171584. 3.4

B. Machenhauer and E. Rasmussen. *On the integration of the spectral hydrodynamical equations by a transformmethod by Bennert Machenhauer and Erik Rasmussen.* Københavns Universitet. Institut for teoretisk meteorologi. Report no.3. 1972. URL http://books.google.de/books?id=MOLCcQAACAAJ. 4.2

C. McLandress, W. E. Ward, V. I. Fomichev, K. Semeniuk, S. R. Beagley, N. A. McFarlane, and T. G. Shepherd. Large-scale dynamics of the mesosphere and lower thermosphere: An analysis using the extended Canadian Middle Atmosphere Model. *Journal of Geophysical Research: Atmospheres*, 111(D17):n/a–n/a, 2006. ISSN 2156-2202. doi: 10.1029/2005JD006776. URL http://dx.doi.org/10.1029/2005JD006776. 4.4

A. J Simmons and D. M. Burridge. An Energy and Angular-Momentum Conserving Vertical Finite-Difference Scheme and Hybrid Vertical Coordinates. *Monthly Weather Review*, 109, 1981. 4.2

Anne K. Smith, Daniel R. Marsh, Martin G. Mlynczak, and Jeffrey C. Mast. Temporal variations of atomic oxygen in the upper mesosphere from SABER. *Journal of Geophysical Research: Atmospheres*, 115(D18):n/a–n/a, 2010. ISSN 2156-2202. doi: 10.1029/2009JD013434. URL http://dx.doi.org/10.1029/2009JD013434. 4.7

Gary E. Thomas and Knut Stamnes. *Radiative Transfer in the Atmosphere and Ocean.* Cambridge University Press, 1999. URL http://dx.doi.org/10.1017/CBO9780511613470. 2.1, 2.1

Benjamin Wolf. Parametrisierung orographischer Schwerewellen. Master's thesis (Diplomarbeit), Universität Rostock, Germany, February 2013. 4.2

X. Zhu. Radiative Damping Revisited: Parameterization of Damping Rate in the Middle Atmosphere. *Journal of Atmospheric Sciences*, 50:3008–3021, September 1993. doi: 10.1175/1520-0469(1993)050<3008:RDRPOD>2.0.CO;2. 2.7, 4.7

Danksagung

Lieber Erich, ich möchte mich bei dir bedanken, dafür das du mich ermutigt hast meine Masterarbeit in der Theorieabteilung des IAP zu schreiben und für die freundliche Aufnahme in selbige. Deine Anregungen und geduldigen Erklärungen haben mir bei der Erstellung dieser Arbeit sehr geholfen.

Lieber Jens, vielen Dank für die anregenden Diskussionen und aufmerksamen Korrekturen zu dieser Arbeit. Die gemeinsam täglich in Freundschaft verbrachten Stunden haben mir sehr viel Freude bereitet.

Lieber Benjamin, liebe Corinna und liebe Annekatrin, vielen Dank für freundschaftlichen Rat und die vielen Hilfestellungen zu meiner Arbeit in den vergangenen Monaten.

Ein großer Dank gilt allen Mitarbeitern des IAP für die angenehme Atmosphäre am IAP und die sehr guten Arbeitsbedingungen.

Liebe Familie, vielen Dank für die andauernde Unterstützung.

Eidesstattliche Erklärung

Ich, Erik Jeglorz, Matrikel-Nr. 8201290, versichere hiermit, dass ich meine Masterarbeit mit dem Thema

> *Long-wave radiative transfer in the middle atmosphere interacting with gravity waves and thermal tides*

selbständig verfasst und keine anderen als die angegebenen Quellen und Hilfsmittel benutzt habe, wobei ich alle wörtlichen und sinngemäßen Zitate als solche gekennzeichnet habe. Die Arbeit wurde bisher keiner anderen Prüfungsbehörde vorgelegt und auch nicht veröffentlicht.

Rostock, den 25. März 2014

Erik Jeglorz

A Anhang

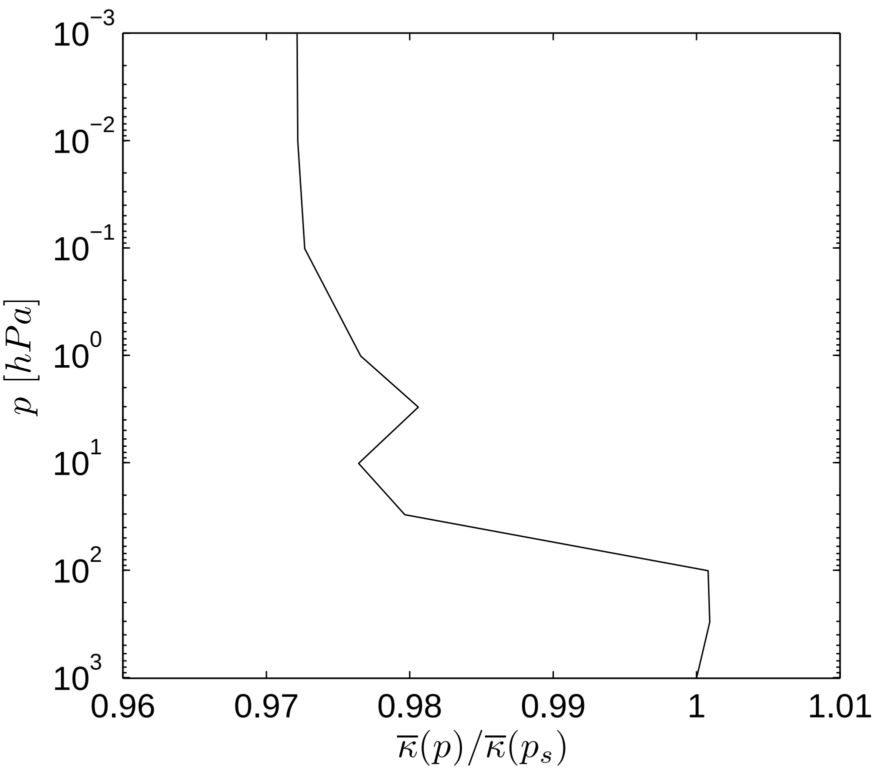

Figure A.1: It is shown the ratio of frequency averaged mass extinction coefficients $\overline{\kappa}(p)/\overline{\kappa}(p_s)$ for the important CO_2 $15\,\mu$m band. The surface pressure is denoted by p_s. The line-by-line integration ($13.3\,\mu\text{m} \leq \nu \leq 16.7\,\mu\text{m}$) was performed with the web interface of the HITRAN database for $T = 250$ K and the gas mixture "USA model, tropics". The variation of $\overline{\kappa}$ with decreasing p is less then 3% over the whole pressure domain. Thus, the dependency on temperature (up to 30% [Knöpfel and Becker, 2011]) is stronger.

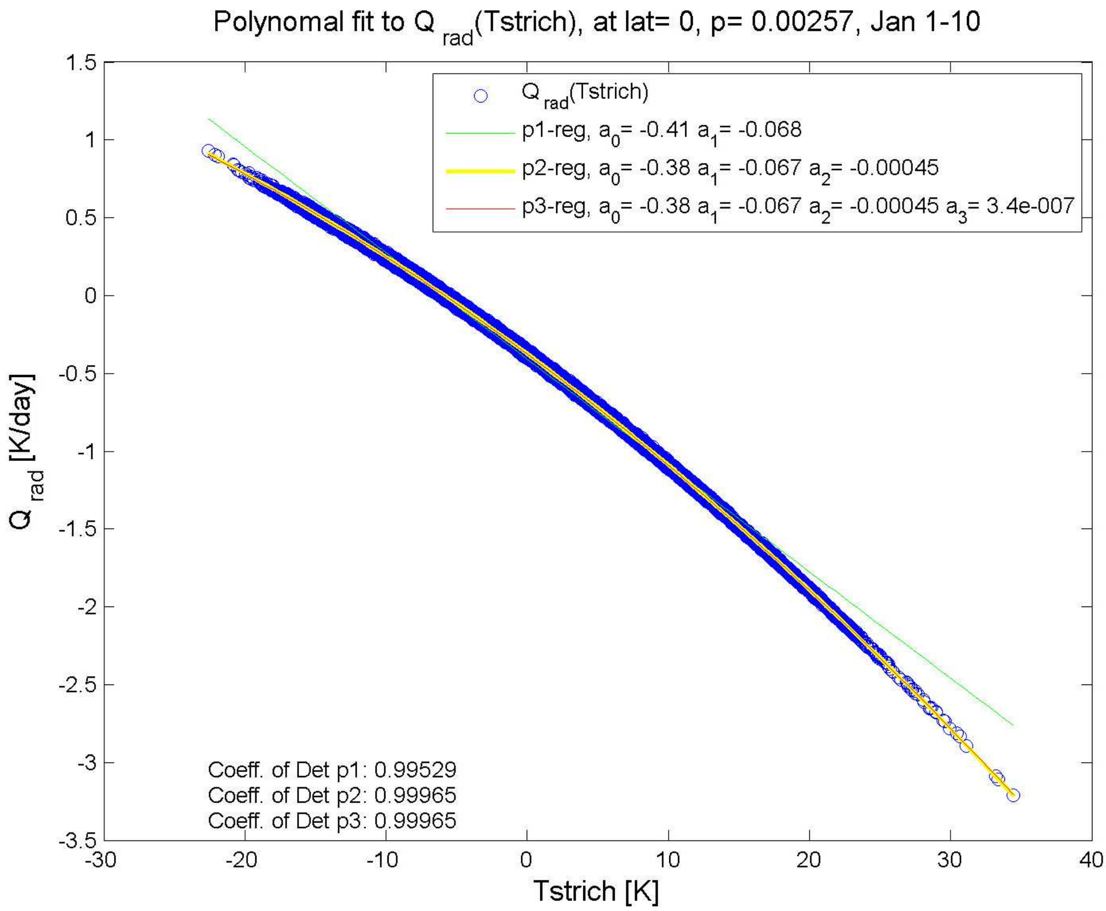

Figure A.2: An example of the fitting curve procedure for 0.0026 hPa at the equator in January. Polynomial fits are tested up to the order of three. One blue circle represents one data point out of the data set $[Q_{\rm rad};\, T'](\lambda, t)$. Latter contains 96 points of a latitude circle for 80 time steps and five model years (38400 single points).

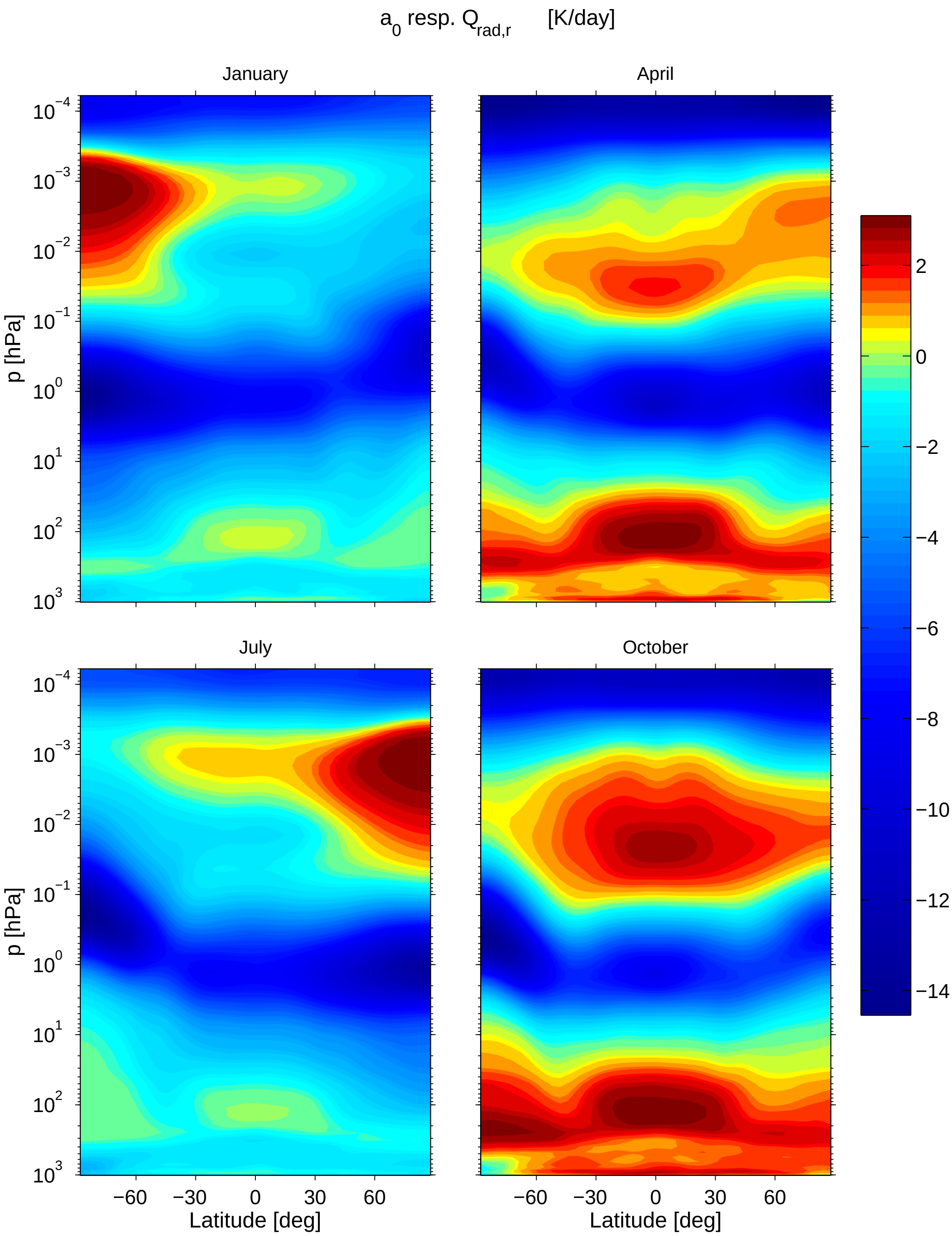

Figure A.3: The curve-fitting parameter a_0 that approximatly represents $Q_{\mathrm{rad,r}}$ as a function of latitude and altitude for different seasons obtained from KMCM simulations.